PHYSICAL REVIEW B VOLUME 24, NUMBER 6 15 SEPTEMBER 1981

Phonon-wind-induced anisotropy of the electron-hole droplet cloud in Ge

M. Greenstein and J. P. Wolfe
Physics Department and Materials Research Laboratory, University of Illinois at Urbana-Champaign, Urbana, Illinois 61801
(Received 19 January 1981)

We report the results of experimental studies of the electron-hole droplet cloud in Ge and present a set of model calculations explaining the anisotropic features of the cloud in terms of a phonon-wind force. Luminescence images of the droplet cloud in Ge display several prominent features: broad ⟨111⟩ lobes, sharp axial ⟨100⟩ flares, and sharp {100} planar flares. The central lobes are identified with the LA-phonon component of the phonon-wind force, while the axial flares are associated with the slow TA component and the planar flares with the fast TA component. Thus, the effects of all three acoustic-phonon modes are observed in the cloud. The anisotropy of the calculated phonon-wind force is due to both the electron-phonon interaction and the ballistic phonon flux. The relative contributions of these factors are examined. Droplet trajectories under the influence of the phonon-wind force are calculated; these calculations illustrate the nonradial nature of the force. All of the general features of the observed anisotropic cloud are well accounted for by the anisotropies of the phonon wind.

I. INTRODUCTION

The motion of photoexcited carriers in semiconductors has been investigated extensively for several decades. At room temperature and in the absence of applied fields, these carriers undergo a diffusive motion due to their strong coupling with thermal phonons. At low temperatures electrons and holes are bound into free excitons (FE), and in high-purity crystals the motion of these neutral particles is also diffusive. In the last decade a new aspect of the motion of photoexcited carriers in semiconductors has emerged. The motion of another photoexcited phase—the electron-hole liquid—is found to be driftlike rather than diffusive. At low temperatures and sufficient excitation levels, photoexcited carriers condense into droplets of this quantum fluid. In Ge the electron-hole pair density of the liquid is 2.2×10^{17} cm^{-3}, and this liquid phase generally takes the form of macroscopic electron-hole droplets (EHD), each containing 10^7–10^8 pairs. Owing to their large mass, droplets are expected to diffuse very slowly. Measurements of the spatial distribution of EHD, as described in detail in this paper, give clear evidence that the intrinsic transport of EHD is instead determined by a flux of nonequilibrium phonons—the phonon wind.

The basic ground-state properties of the electron-hole liquid have been explained in the last decade; for Ge and Si there is generally good agreement between theoretical predictions and the many experimental observations.[1] Most of the experimental work on the electron-hole liquid has been performed in Ge because of the relatively long intrinsic lifetime of the liquid $\tau_0=40$ μs, and the high purity of present-day Ge samples. For these reasons, Ge is also a prime candidate for measuring the macroscopic motion of EHD and FE.

The spatial extent of the liquid in Ge has been investigated previously[1] by observing the EHD recombination luminescence and by light-scattering techniques. These experiments showed that with surface excitation, a cloud of droplets, each droplet with a 2–10 μm radius, is formed. The size of the cloud is dependent on excitation level and can be several millimeters in extent, with an average density of about 1% that of a single drop. The basic question raised by the observation of these large clouds is how such massive droplets move these large distances within their lifetime. At low temperatures droplet motion is strongly damped by collisions with thermal phonons; therefore, EHD can travel ballistically only very short distances. The momentum damping time of a droplet due to this electron-phonon scattering has been determined, for example, by acoustic attenuation,[2] to be $\tau_p\simeq10^{-9}$ s at 4 K. This implies a diffusion constant $D=\tau_p k_B T/M\approx10^{-4}$ cm^2/s. Here M is an appropriate inertial mass per pair for the drops (Ref. 3), $M=0.97m_0$, with m_0 the free-electron mass. Thus thermal diffusion of these relatively massive droplets yields a net displacement of $l\simeq\sqrt{D\tau_0}\simeq1$ μm in their lifetime of 40 μs. This displacement is far too small to account for the observed size of the droplet cloud in Ge.[4]

In addition to the large cloud sizes, there are three other experimental indications that the transport process is not diffusive: (a) Both light-scattering[5,6] and luminescence studies[7] have shown that the cloud radius is strongly dependent on laser excitation power, while the droplet radius is observed to be only weakly power dependent. (b) For a wide range of excitation levels, the average density in the cloud is observed to be approximately con-

stant. (c) The velocity distribution of droplets within the cloud, as determined by laser Doppler velocimetry,[8] is characteristic of rectilinear particle motion, not diffusive motion. These experimental observations argue convincingly against simple diffusion as the transport mechanism.

To move EHD macroscopic distances a net force is therefore required. For an applied force $\vec{F}$, droplets move with a drift velocity defined by the drift relation

$$\vec{V}_D = \frac{\tau_p}{M}\vec{F}. \tag{1}$$

In 1975, Keldysh and co-workers[9,10] proposed the idea that a nonthermal phonon flux—a phonon wind—could provide the required force. The central idea is that acoustic phonons with a wave vector less than twice the Fermi wave vector are absorbed by EHD, due to the deformation-potential interaction, thus producing a net momentum transfer to the droplets.

This phonon-wind idea forms the basis for the current view of droplet transport. Our experiments on the spatial structure of the cloud have led to a schematic view of the cloud shown in Fig. 1. Since the excitation photon energy typically has much higher energy than the band gap, hot photoexcited carriers are produced in the excitation region. These hot carriers cool by the emission of phonons. Initially, rapid carrier thermalization

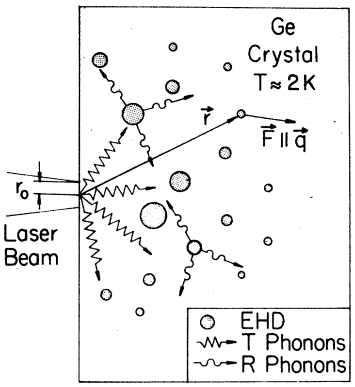

FIG. 1. Schematic view of an EHD cloud produced by focused-surface excitation. Droplets are produced very near the excitation region. As they decay, the droplets are pushed by phonons along drift trajectories into the crystal. Two distinct sources of phonons are illustrated. Thermalization (T) phonons emanate from the localized excitation region, whereas recombination (R) phonons are generated by EHD throughout the cloud volume. An EHD at position $\vec{r}$, which absorbs a T phonon with group velocity $\vec{V}=|\vec{V}|\hat{r}$, is subject to a force $\vec{F}$ along the phonon momentum $\hbar\vec{q}$. As discussed in Sec. IV, this force is generally nonradial because $\vec{V}$ and $\vec{q}$ are generally noncollinear.

occurs by the emission of LO phonons on a 100 ps time scale.[11,12] A localized source of long-wavelength acoustic phonons can arise from both the downconversion of these optical phonons as well as from direct acoustic-phonon emission by the hot carriers in the final stages of the thermalization process. (When the carrier kinetic energy is less than the minimum energy of an optical phonon, further thermalization requires the direct emission of acoustic phonons.) We refer to phonons which are a byproduct of the photoexcited free-carrier thermalization process as T phonons. In this paper we are concerned mainly with those T phonons with the long wavelength required to push droplets. The source of these T phonons is expected to be localized to very near the excitation region. Once thermalized, the photoexcited carriers condense into EHD close to the excitation region. The EHD are thus continuously bombarded by a phonon flux emanating from the thermalization region, and are pushed along drift trajectories into the bulk of the crystal. As they drift, the droplets decay in their natural lifetime $\tau_0 \simeq 40$ μs. Owing to Auger recombination, EHD are also copious sources of long-wavelength acoustic phonons. This source of phonons, recombination (R) phonons, is more diffuse and distributed throughout the cloud volume.

With the aid of a steady-state continuity equation these ideas can be put into a more quantitative form. At any point away from the excitation region, the droplet-flux density is the product of the local cloud density $n(\vec{r})$ and the droplet velocity $\vec{V}_D(\vec{r})$, implying

$$\vec{\nabla}\cdot(n\vec{V}_D)+n/\tau_0=0. \tag{2}$$

Keldysh and co-workers solved this continuity equation with the boundary conditions $n(r=0)=\bar{n}$ and $n(r=\infty)=0$, and under the assumption that the effects of diffusion could be neglected; i.e., assuming the drift relation from Eq. (1),

$$n\vec{V}_D = n\frac{\tau_p}{M}\vec{F}. \tag{3}$$

From Eqs. (2) and (3) we have

$$\frac{\tau_p}{M}\vec{\nabla}\cdot(\vec{F}n)+\frac{n}{\tau_0}=0. \tag{4}$$

The solution to this equation in three dimensions, obtained by Keldysh for the given boundary conditions, and a radial inverse-square-law force, yields a density

$$n(r)=\bar{n}e^{-r^3/\lambda^3}. \tag{5}$$

The effective exponential length λ is given by

$$\lambda^3=\frac{3\tau_0\tau_p}{M}w, \tag{6}$$

with the phonon-wind flux w defined by

$$\vec{F}=\frac{w}{r^2}\,\hat{q}\ . \tag{7}$$

The inverse-square-law dependence is due to the geometric reduction of the phonon flux with distance from a point source. The phonon-wind force was estimated in Ref. 10 for excitons and EHD assuming an approximate form for the nonequilibrium phonon distribution function. These calculations took the various anisotropic factors of the force as simple isotropic averages.

It can be easily shown that the solution, Eq. (5), still holds for an anisotropic radial force, i.e., $w=w(\theta,\phi)$. However, this solution does assume that the force is radial ($\hat{q}=\hat{r}$). As indicated in Fig. 1, this is not strictly true since $\hat{q}$ is generally nonradial due to phonon focusing effects, as discussed in Sec. IV. Nevertheless, a radial force is a useful first approximation which will later be used in the calculations of the cloud shape.

This simple theory makes an important prediction. From Eqs. (5)–(7) it is clear that the effective cloud volume λ^3 is proportional to the phonon-wind flux. The nonequilibrium phonon flux is, in turn, assumed to be proportional to the number of free carriers produced by photoexcitation. It is commonly observed that, at moderate excitation levels, the total number of photoexcited free carriers depends linearly upon excitation power. This observation, in conjunction with Eqs. (5)–(7), gives the isotropic-phonon-wind theory of Keldysh and co-workers an important experimentally observable prediction: the cloud volume increases linearly with the excitation power. Both luminescence and light-scattering experiments support this prediction.

With the publication of the isotropic-phonon-wind theory of Keldysh and co-workers, several experimental groups began to look closely at the interaction of nonequilibrium phonons with EHD. Experiments dealing with the steady-state cloud may be grouped into two categories: (1) those investigating the effects of phonons generated outside the cloud (external phonons), and (2) those investigating the phonons generated within the cloud, i.e., phonons directly responsible for the cloud formation (internal phonons).

In their original paper, Bagaev *et al.*[10] showed that external phonons (produced by another laser) could displace a droplet cloud. Hensel and Dynes[13] further demonstrated the attenuation of heat pulses by a droplet cloud, and at high flux levels they were able to induce an observable drift of the EHD. To study the internal-cloud mechanism Doehler and Worlock[8,14,15] used a velocimetry technique to map the radial-velocity distribution in small clouds. Also, in further experiments, they were able to observe small increases in the droplet velocities when the carriers in the droplets were heated by an external source of infrared (2 μm) radiation. These latter experiments indicated a small effect of R phonons on the droplet velocities.

Using an early version of the imaging system described in this paper, we[16] produced the first infrared image of an anisotropic EHD cloud in Ge. This experiment, which initially revealed the spatial anisotropy of the cloud, unequivocally demonstrated that an internal-phonon-wind force, emanating mainly from the excitation region, is responsible for the intrinsic transport of EHD and the formation of the cloud. As will be shown in Sec. III, the steady-state anisotropic cloud in Ge, produced by continuous focused-laser excitation, consists of broad lobes along the $\langle 111\rangle$ directions, sharp axial flares along the $\langle 100\rangle$ directions, and very sharp planar flares in the $\{100\}$ planes.

Before these imaging experiments the distribution of droplets emanating from a point excitation source was generally assumed to possess at least cylindrical symmetry. This type of distribution would be reasonable if droplets were diffusing into the crystal or if there existed repulsive electrostatic forces between droplets—two possibilities which were postulated. On the other hand, anisotropy is a natural consequence of the phonon-wind force. The electron-phonon interaction is highly anisotropic, and, depending on its origin, the phonon flux may also be anisotropic. It is important to realize, however, that the degree of anisotropy depends quite strongly on the *source* of the phonons. Indeed, the situation originally suggested by Keldysh[9] (R phonons) would likely provide very little cloud anisotropy. Consequently, the possibility that the cloud might be anisotropic was not immediately recognized after Keldysh's phonon-wind proposal. Owing to the complexity of the factors in the phonon-wind force (i.e., undetermined source of phonons, phonon-flux distribution, and EHD-phonon interaction), it would not have been easy to predict if the cloud was isotropic or not. Thus, the observation of an anisotropic cloud accomplished two ends: (1) it revealed that a direction-dependent drift force was pushing droplets into the crystal, and (2) it demonstrated that an important source of this drift force was localized at the excitation region. The cloud shape was, in addition, qualitatively explained by considerations of the electron-phonon coupling and phonon focusing. These experiments demonstrated for the first time the essential role of a directed phonon flux in creating the droplet cloud.

The prominence of T phonons for the present

case of EHD clouds in Ge is also supported by the theoretical calculations of Markiewicz,[11,17] and by quantitative experimental observations of the build-up and decay of the cloud.[18] This dominance of the phonon-wind force by the T phonons is not, however, a necessary fact. Indeed, the EHD distribution in silicon provides a counter example; no strong anisotropy is observed in the EHD cloud in Si.[19] The lifetime of EHD in Si, is much shorter, about 140 ns. Thus, the cloud is quite small and the R-phonon generation rate is greatly enhanced. The diffuse nature of this source of phonons would not be expected to create sharp anisotropies in the cloud.

As illustrated in Fig. 1, T phonons emanating from the excitation region with group velocity $\vec{V} = |\vec{V}|\hat{r}$ are absorbed by a droplet at position $\vec{r}$. The phonon is absorbed by a carrier within the droplet and fast carrier-carrier interactions transfer the absorbed energy and momentum to the droplet as a whole. Thus, a force along $\hbar\vec{q}$ results. It is important to note that for the phonons, $\vec{V}$ and $\vec{q}$ are generally noncollinear. This is a subtle, yet very important point that comes from phonon-focusing theory and is due to the elastic anisotropy of the crystal. This noncollinearity gives a nonradial character to the phonon-wind force, to be discussed in detail in Sec. IV. In addition, because of this noncollinearity, the phonon-wind forces calculated as a function of $\hat{q}$ must be transformed into the direction $\hat{V} = \hat{r}$ for comparison with real-space observations. This transformation is generally not trivial.

In this paper we present the results of extensive experimental studies of the spatial distribution of EHD in the cloud, and give a set of model calculations which reveal the various factors in the phonon-wind force. Experimentally, the spatial distribution of droplets in the cloud is examined as a function of the important experimental parameters in Sec. III. We consider theoretically both the anisotropic electron-phonon coupling and the angle-dependent phonon flux emanating from a point source in Sec. IV.

II. EXPERIMENTAL METHODS

Most of the intrinsic properties of the electron-hole liquid have been experimentally determined from the recombination luminescence. Since Ge has an indirect band gap, a phonon is required to conserve crystal momentum during a recombination event, and the emission spectrum of the liquid in Ge is characterized by several phonon replicas. The recombination photon energies are determined primarily by the energy gap at low temperature (744 meV), minus the L-point phonon energies (TO, LO, LA, TA; 39, 30, 27, 9 meV) and the electron-hole liquid ground-state energy[20] (6 meV), or the free-exciton binding energy[21] (4.2 meV). A typical spectrum taken at $T = 4.2$ K is shown in Fig. 2. Both the liquid and the FE lines are observed. The LA phonon replica of the liquid, at 709 meV (1.75 μm), is the most intense liquid emission line. At lower temperatures ($\lesssim 2$ K) the exciton line is no longer observed because the nonequilibrium carriers are almost entirely condensed into the liquid phase. Most of the luminescence imaging experiments reported here were conducted at $T \lesssim 2$ K.

In the present study we image the characteristic recombination emission at 1.750 and 1.738 μm to determine the spatial properties of the electron-hole liquid and free-excitons, respectively. This type of experiment presents some special difficulties which must be overcome. In the first place, a rather high sensitivity is required. To characterize the cloud of droplets, we divide the region of the cloud into a two-dimensional grid of spatially distinct elements. For example, if a 256×256 element array spans the region of the cloud, then each element radiates, on the average, only $2^{-16} = 1.5 \times 10^{-5}$ of the total number of photons emitted from the entire cloud. Second, each of these elements must be sampled relatively quickly so that an entire image (2^{16} elements) may be observed within a reasonable period of time. This is par-

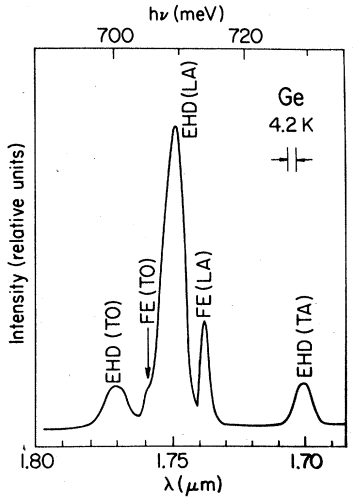

FIG. 2. Typical luminescence spectrum showing the major phonon replicas of both the electron-hole liquid and free-exciton phases for focused excitation at an incident power of 50 mW in Ge at 4.2 K. The strongest line, the LA-phonon replica, is used in all of this work. The relative intensity of the EHD and exciton lines at 4.2 K is a function of both excitation power and focus. At $T \approx 2$ K, where most of the data in this paper were taken, no FE luminescence is observable.

ticularly important in those experiments where a number of experimental parameters (e.g., image focus, laser focus and position, excitation power, etc.) must be jointly optimized by observing the image. To output an image within, for example, 20 s, a detector response of less than a millisecond is required. Finally, a method is required to store and handle the immense amount of information contained in a single image. For comparison to theory, each image element (pixel) must contain a signal proportional to the number of detected photons over a very large dynamic range.

The radiative efficiency of the electron-hole liquid is rather high, on the order of 25%; however, the near-infrared wavelengths ($\lambda = 1.75$ μm) are well outside the detection limits of commercially available photomultiplier devices. A TV vidicon tube with an ir-sensitive (PbS) surface has previously been used to image single large EHD produced by strain-confinement methods.[22] The luminescence intensity from a strain-confined drop, however, exceeds that emitted from a cloud of small EHD by one to two orders of magnitude. A commercial vidicon that we tried had insufficient sensitivity for our cloud studies. In addition, the vidicon has an intrinsically nonlinear response, relatively small dynamic range, and offered no opportunity for spectral or time resolution.

The experimental approach we devised, scanning with a single element detector, overcame these difficulties at the expense of losing the multiplex advantage of a detector array. The intrinsic Ge detector we employ has an extremely high sensitivity, a linear response over a wide dynamic range, a time response which is variable from submicroseconds to seconds, and may be naturally coupled to a spectrometer system for spectrally resolved imaging. In addition to permitting rapid spatial scanning, the fast response of this detector is sufficient to produce time resolved "snap shots" of the buildup and decay dynamics of the cloud using a time-resolved slit-scanning technique reported by us elsewhere.[18] The present work, however, deals exclusively with the steady-state distribution of the EHD produced by a continuous laser beam.

The single-element infrared detector we use is a Ge *pin* Schottky diode operated in the photoconductive mode, similar to those developed as energy-resolved particle detectors.[23] The sensitivity of the diode at $\lambda = 1.75$ μm is optimized by adjusting the operating temperature of the diode. The band gap of Ge decreases from 744 meV, at 4.2 K, to 663 meV, at 300 K. We exploit this temperature dependence of the gap by cooling the detector to a temperature of about 200 K where the leakage current is greatly reduced, while the quantum efficiency at 1.75 μm is still quite high. At 200 K, for $\lambda = 1.75$ μm, the optical-absorption length of Ge is approximately the length of the detector crystal, 1 cm. We measure the detectivity of this detector as $D^* = 2\times10^{14}$ cm W^{-1}Hz$^{1/2}$ at $\lambda = 1.75$ μm. When reverse biased between 10–100 V, the dark current is less than 200 pA.

A schematic diagram of the infrared imaging apparatus is given in Fig. 3. A YAG:Nd laser beam is focused onto the Ge sample, which is immersed in liquid helium in an optical cryostat. All data in this paper were obtained in a superfluid He bath at $T = 1.75$ K with a focused YAG:Nd laser as the excitation source, unless otherwise noted. The 1.06-μm wavelength laser light is absorbed within about 1.0 μm of the sample surface. An 85-mm focal length, $f/1.5$ imaging lens focuses the EHD recombination luminescence onto the image plane of a $\frac{1}{4}$-meter $f/3.5$ spectrometer; the image magnification is about 3.0. The Ge photodiode is located at the exit slit of the spectrometer, and the induced photocurrent is amplified by a low noise current preamplifier.

Using this sensitive, single-element detector, images are produced by raster scanning the sharply focused infrared image of the cloud across an aperture at the entrance of the spectrometer. A microcomputer controls the optical-scanning experiment by applying voltages to two precision galvanometers which rotate two deflection mirrors about orthogonal axes.[24] In this way the image can be *xy* translated across the entrance aperture. Typical scan frequencies are 20 Hz horizontal and 0.01 Hz vertical. The detector aperture width ranges from 150 to 500 μm, providing an effective spatial resolution at the sample of 50 to 170 μm. Images are typically acquired in 3–5 min depending upon the amount of signal averaging required. To quickly ascertain the gross features of the cloud or simply optimize the optics, a complete image is frequently not necessary. By replacing

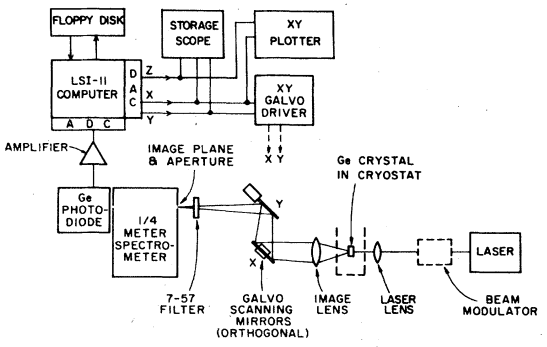

FIG. 3. Schematic diagram of the computer-controlled infrared imaging system, capable of spatial, spectral, and time resolution.

the aperture with a slit, integration over one dimension is affected, and a scan of the image perpendicular to the slit axis (a slit scan) can be used to determine a spatial profile of the cloud as some external variable is changed. This slit-scan technique has been used by other workers.

Data acquisition and display are controlled by the microcomputer as indicated in Fig. 3. The cloud image is written onto a floppy disk in a 256×256 element array through an eight-bit analog-to-digital converter. Typically, four images fit on each side of a floppy disk. To display the digitized images, the contents of the array are written, through a digital-to-analog converter, onto an x-y storage oscilloscope with the digitized luminescence signal modulating the z axis (intensity) of the oscilloscope. The slit-scan data are acquired in an analogous manner with the y mirror held stationary. The slit-scan data are displayed on an x-y plotter or an oscilloscope. By digitizing the cloud images we are able to do extensive quantitative analysis on the cloud shape. Several examples of this type of analysis are given in Sec. III. The calculations of Sec. IV were also performed on this same microcomputer.

The Ge samples used in this investigation are ultrapure and dislocation free.[25] The net impurity content of these uncompensated crystals is $N_A \sim 2 \times 10^{11}$ cm^{-3}. A knowledge of the dislocation density and distribution of dislocations in the sample is important: We have discovered that dislocations provide a strong perturbation on the cloud shape.[26] The local strains associated with a dislocation scatter EHD and perturb the intrinsic phonon-wind-determined flow pattern of droplets in the cloud. A single dislocation line actually presents an effective scattering width of approximately 100 μm to EHD. Indeed, at dislocation densities above 10^4 cm^{-2}, the cloud anisotropy was found to be completely washed out. Thus, dislocation density cannot be ignored in EHD transport studies.

Excitation surfaces were either chemically etched or mechanically polished.[27] The etched surfaces allow for a higher EHD production efficiency ($3\times$), but the polished faces result in a better definition of the excitation surface when the viewing direction is along this surface (sideview). Except for regions near the surface, the etched and polished excitation surfaces produce similar cloud shapes. The effects of polished versus etched excitation surfaces on the cloud will be discussed in detail in Sec. III.

III. EXPERIMENTAL RESULTS

A. General features of the cloud

As mentioned in Sec. I, the isotropic-phonon-wind theory forwarded by Keldysh in conjunction with the linear dependence of the free-carrier generation rate on excitation power, contains an important observable prediction: the cloud volume will increase linearly with excitation power. This property has been previously observed in both luminescence work[5,6] as well as light-scattering studies.[7] We begin by presenting data which confirms this power law for our experimental conditions which produce the anisotropic steady-state cloud.

Figure 4(a) gives a representative set of slit-scan

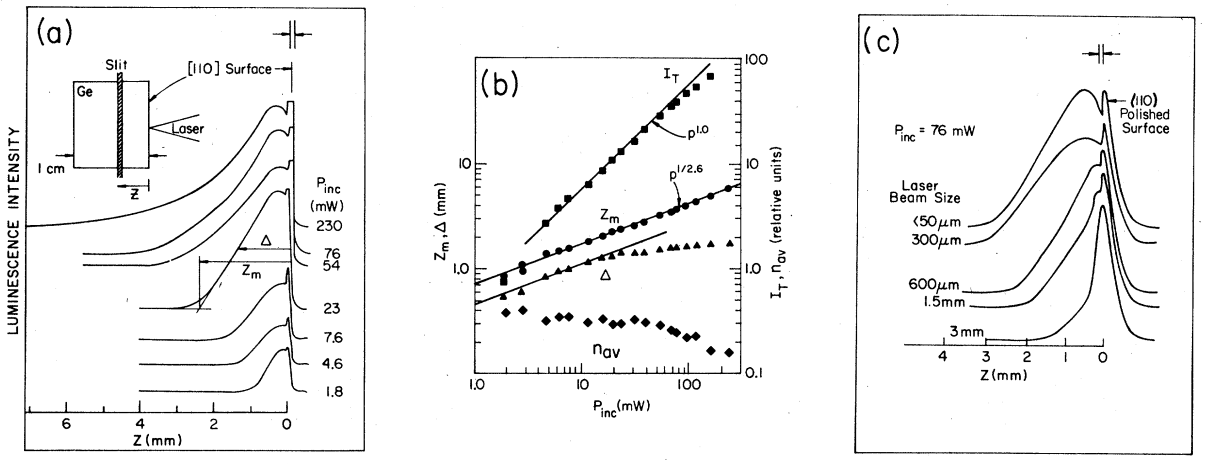

FIG. 4. (a) Slit-scan traces showing incident power dependence of the cloud extent for an etched (110) excitation surface viewed along [001]. The intensities at the crystal edge have been truncated for clarity. (b) A plot of the power dependence of the integrated intensity I_T, the penetration depth Z_m, the spatial full width Δ, and the average density $n_{av} \equiv I_T/Z_m^3$. Note that Δ and Z_m are defined in (a). The cloud volume Z_m^3 increases approximately linearly with excitation power as predicted. (c) Laser-focus dependence at $P_{inc} = 76$ mW for a polished (110) surface.

traces (cloud profiles) showing the expansion of the cloud with increased excitation power. The excitation surface, an etched (110) surface, is seen as a sharp intensity peak at the right. This peak is produced by EHD luminescence emanating from the bulk of the crystal and scattered from the surface. In the figure some of these sharp-edge signals are truncated for clarity. The droplet cloud is observed to penetrate up to several millimeters into the Ge sample, and, under these focused-laser conditions, the peak of EHD intensity is actually well inside the crystal for the higher excitation powers. In addition, the cloud profile changes shape, acquiring a long tail at higher powers. In Fig. 4(a) the full width Δ and the penetration depth Z_m of the cloud profile are defined. As shown in Fig. 4(b), the total integrated intensity $I_T \equiv \int I(z)dz$, which is proportional to the total number of electron-hole pairs in the liquid phase, is found to depend linearly upon excitation power. The penetration depth Z_m, a measure of the cloud size, depends on power as $P^{1/2.6}$. This is close to the $P^{1/3}$ value predicted for the cloud radius from the isotropic-phonon-wind model. The full width Δ follows Z_m up to about 20 mW where it begins to level off. This is near the power where the shape of the cloud profile gradually changes. The average cloud density, defined as $n_{av} \equiv I_T/Z_m^3$, is observed to be roughly constant.

The importance of the size of the excitation spot, or laser focus, for the cloud extent is illustrated in Fig. 4(c). This set of data is obtained for a polished (110) excitation surface. Similar results are obtained for an etched excitation surface. As the excitation density is reduced by increasing the size of the laser spot, the penetration depth becomes greatly reduced, and the point of maximum intensity approaches the excitation surface. Thus, the size of the excitation region has an important bearing on the cloud size: droplets are pushed much farther into the crystal for a concentrated excitation region. In this figure the gain of the x-y recorder is held constant. This implies that as the laser is defocused, the total number of EHD produced is actually reduced. We attribute this to surface traps. For the defocused-excitation source the effect of surface traps will be enhanced because the effective surface area is increased. The importance of focus for the cloud shape will be discussed shortly. Unless otherwise noted, all cloud images are taken with a ~100-μm excitation spot size.

Another interesting effect of high excitation density is observed. Under focused-excitation conditions in a superfluid He bath, a helium gas film or bubble, can occur on the crystal surface at the excitation spot. The size of the film depends on the laser power density, and the liquid-He pressure. As the laser is defocused, a power-density threshold of approximately 100 W/cm^2 is reached at which the bubble vanishes. With the disappearance of the bubble, the cloud profile collapses significantly toward the crystal surface. This transition occurs in Fig. 4(c) between excitation region diameters of 300 and 600 μm. In addition, this He bubble oscillates in time and displays a hysteresis phenomenon in the threshold power density. The gas bubble is present in all of the highly focused-excitation experiments reported in this paper. We believe that this He bubble effectively increases the thermal impedance between the sample and the He bath at the excitation point, and as such, enhances the phonon-wind force by reducing the transmission coefficient of phonons into the superfluid liquid-He bath.[28] We have also observed this bubble on a variety of materials (e.g., Ge, Si, Al, and Au). The threshold for nucleation of the He gas bubble is not particularly sensitive to the material excited by the laser. The lifetime of the gas bubble after the light is switched off is on the order of 10–50 μs, similar to the observed duration of the "hot spot" postulated by Hensel and Dynes.[13] Our data indicate, however, that the gas bubble and the hot-spot effect are really two distinct phenomena.

B. Excitation conditions: The droplet-to-phonon ratio

We now return to the subject of etched versus polished excitation surfaces, and also include a discussion of the differences between YAG:Nd and Ar^+ excitation sources. The common theme here is the ratio of the strength of the phonon-wind force to the number of electron-hole pairs in the cloud. Both the excitation surface preparation and the excitation photon energy give us a probe of this important ratio. These kinds of comparisons permit a careful examination of the source of the phonon-wind force, and strongly support the idea that the phonon-wind force arises mainly from a localized source of thermalization phonons.

1. Effect of surface condition

It is generally observed that chemical etching of a crystal-excitation surface enhances the luminescence from EHD. In Fig. 5 we illustrate the spatial effects of etched and polished excitation surfaces for YAG:Nd excitation with two sets of cloud profiles. The reflectivity and, therefore, the absorption of the two surfaces is measured to be the same to within 5%. In Fig. 5(a) two incident powers were selected that produced equal penetration depths. According to our simple model [Eqs.

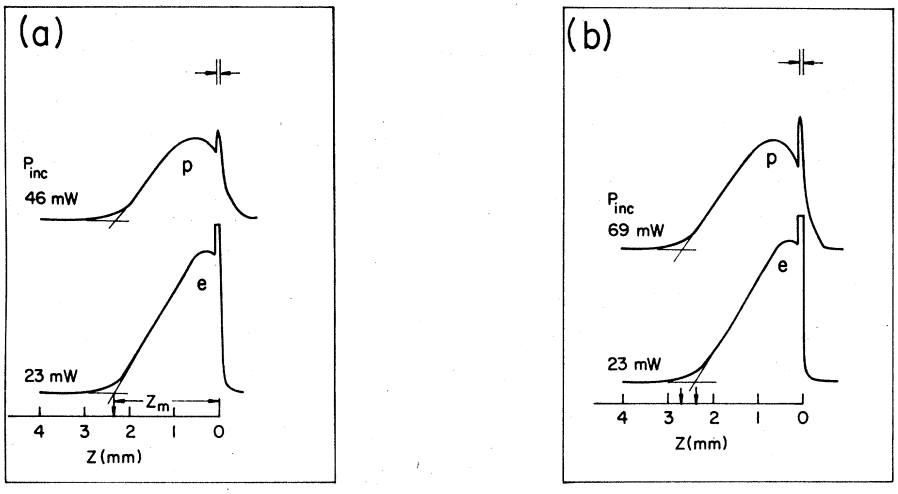

FIG. 5. Cloud profiles showing comparison of etched and polished (110) excitation surfaces for YAG:Nd excitation. (a) At constant penetration depth Z_m. (b) At constant number of e-h pairs in the cloud.

(5)–(7)] this implies equal phonon-wind strengths in the two cases. To obtain these equal cloud sizes, twice as much power is required on the polished surface. However, under these conditions, pumping the etched surface yields a cloud with approximately 1.5 times more pairs, implying a higher droplet-to-phonon ratio for this surface. If instead, we choose two clouds with equal number of e-h pairs (equal total integrated intensity), as in Fig. 5(b), we observe that it requires 3 times the power on the polished surface to create an equal number of pairs, while the cloud extent is increased by only a factor of 1.12. We conclude then that both droplets and the phonon wind are created less efficiently with a polished rather than with an etched surface.

Figure 5 also illustrates that the two surface conditions yield cloud profiles with different shapes near the excitation surface. A significant drop in luminescence intensity is observed near the polished excitation surface, which we attribute to nonradiative recombination, enhanced by deep surface damage. Raman studies in semiconductor samples have shown that high-frequency phonons are also sensitive to the damaged layer caused by mechanical polishing.[29] The depth of this layer is found to be on the order of the final grit size, in our case[27] this is 1 μm.

In order to examine the effect of this damaged layer more quantitatively, we present in Table I a set of ratios (etched to polished) for the basic parameters of the cloud. These numbers are the ratios of the absorbed photon flux R_F, the total number of EHD in the cloud R_I, the penetration depth R_z, the density R_n, and the force per pair in the cloud R_0. This last ratio is defined as the inverse of R_n. (Recall that in the simple phonon-wind model, the cloud density is independent of excitation level.) These ratios are given for both YAG:Nd ($h\nu = 1.16$ eV) and Ar^+ ($h\nu = 2.41$ eV) excitation sources, and are the average values obtained from a set of traces over a wide range of powers where cloud shapes are similar. Both lasers are included here to demonstrate that the difference in absorption lengths, about 0.02 μm for Ar^+ and about 1.0 μm for YAG:Nd does not alter the results significantly. (This is further evidence that the damaged layer is at least 1 μm in extent.) For each row in the table, one ratio is set equal to 1 and the other ratios are calculated from the appropriate slit-scan traces. For constant Z_m ($R_z = 1.0$), pumping the etched surface with half the photon flux creates a comparable force, but this phonon flux also creates 1.5 times as many pairs. For equal fluxes ($R_F = 1.0$) the EHD production efficiency on the etched surface is 3 times that of the polished surface. To create an equal number of pairs ($R_I = 1.0$) on the etched surface requires $\frac{1}{3}$ the power and yet a cloud is created with 0.89, the

TABLE I. Ratios (etched-to-polished) of various parameters for both YAG:Nd and Ar^+ excitation on a (110) surface. The ratios are defined in the text.

	R_F	R_I	R_z	R_n	R_0
YAG:Nd	0.5	1.5	1.0	1.5	0.67
	1.0	3.0	1.3	1.4	0.71
	0.33	1.0	0.89	1.4	0.71
Ar^+	0.5	1.5	1.0	1.5	0.67
	1.0	3.3	1.4	1.4	0.71
	0.33	1.0	0.83	1.7	0.59

extent of that produced on the polished surface. Each of these entries indicate that the average density of the cloud produced on the etched surface is about 1.5 times as great as that produced on the polished surface.

A useful gauge of the relative phonon-wind strength is the ratio of the force to the number of pairs in the cloud. A measure of the force may be obtained from Z_m^3, as indicated in Eq. (6). In the last column the ratios for the force per pair R_0 show that the polished surface produces a stronger phonon-wind force *per e-h pair* in the cloud than does the etched surface. This is a consequence of the fact that the phonon-wind force is apparently reduced by a factor of 2 on the polished surface while the EHD production efficiency is reduced by a factor of 3. We can therefore draw two interesting conclusions from Table I: (1) The phonon-wind force is affected by a damaged layer at the excitation surface extending at least 1 μm in depth. This implies that the phonon-wind force originates mainly from very near the excitation region. (2) The phonon-wind force and the droplet-production efficiency appear to be reduced by different amounts on the polished surface. This experiment shows that the number of droplets and the strength of the phonon-wind force can be altered independently. In contrast, an R-phonon wind is expected to scale directly with the number of droplets.

2. *Effect of excitation photon energy*

Another approach to the problem of determining the source of the phonon-wind force is to attempt to change the thermalization component of the force by altering the excess photon energy[30] $h\nu - E_{gap}$. For Ge, an Ar^+ laser produces 4 times the excess energy of a YAG:Nd laser. A comparison of clouds produced by YAG:Nd and Ar^+ lasers is shown in Fig. 6. In Fig. 6(a) the relative power of the two lasers was selected to give nearly the same penetration depth. The luminescence intensity and hence the cloud density is, however, 1.7 times as large for YAG:Nd excitation. It is important to note here that the relative cloud densities are determined independently of the pumping efficiencies; the luminescence collection efficiency is identical in both cases. These data immediately show that the phonon wind, which determines the cloud size, has an origin other than from the droplets themselves. Figure 6(b) compares the cloud penetration depths obtained when the total number of pairs in the two clouds is about the same. The penetration depth is observed to be about 1.3 times as large for Ar^+ than for YAG:Nd. The cloud shape is also significantly different. The peak of the EHD intensity is much further into the crystal for Ar^+ excitation.

These differences are examined in Table II, with R corresponding to ratios of (Ar^+/YAG:Nd) and the ratios of photon flux, total EHD intensity, penetration depth, EHD density, and force per pair, as in Table I. The relative absorbed photon flux is obtained by multiplying the measured incident power by the reciprocal of the photon energies (1.16/2.41) and by the absorption factors (0.48/0.62) appropriate to Ge at these temperatures.[31] These last two terms give a factor of 2.7 larger absorbed photon-flux per milliwatt of incident power for the YAG:Nd source. The first two rows, for both etched and polished surfaces, indicate that equal

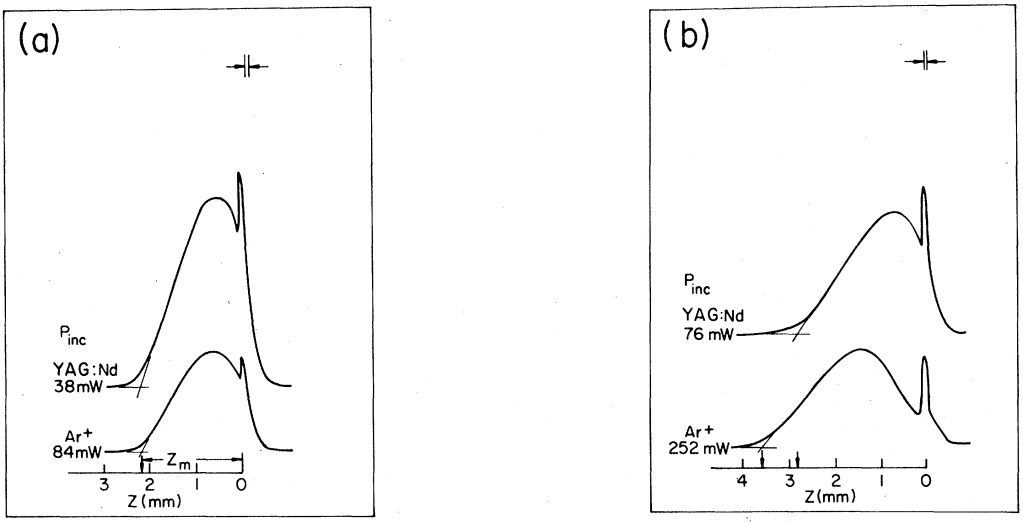

FIG. 6. Cloud profiles showing comparison of Ar^+ and YAG:Nd laser excitation on a polished (110) surface. (a) At constant penetration depth Z_m. (b) At constant number of e-h pairs in the cloud.

TABLE II. Ratios (Ar^+/YAG:Nd) of various parameters for both etched and polished (110) surfaces.

	R_F	R_I	R_z	R_n	R_0
Etched	0.96	0.69	1.0	0.69	1.45
	1.0	0.76	1.03	0.70	1.40
	1.36	1.0	1.22	0.55	1.80
Polished	0.73	0.56	1.0	0.60	1.67
	1.0	0.73	1.10	0.58	1.72
	1.32	1.0	1.18	0.62	1.64

absorbed photon flux apparently produces nearly equal penetration depths.[32] However, the Ar^+ source produces only about 0.75 times as many pairs in EHD. When the number of pairs is set equal, it is observed that the penetration depth is about 1.2 times greater for the Ar^+ source. Thus the Ar^+ source creates a cloud 0.62 times as dense; i.e., with 1.6 times greater phonon-wind-force per pair in the cloud. As previously stated, with the band gap at 0.744 eV the Ar^+ laser has 4 times the excess energy to give to a carrier as kinetic energy. This suggests that for these two laser wavelengths, the flux of phonons due to direct acoustic-phonon emission in the final stage of the thermalization process is comparable. The ratio of the resulting phonon fluxes in these two cases is determined by the details of the thermalization process. At the present time this is not very well understood. We speculate that the difference in EHD production efficiency for these two laser sources may, in part, be related to the difference in absorption length.

Thus we see that the phonon-wind force is sensitive to the condition of the excitation surface in the first few microns and also to the excitation photon energy. The phonon-wind force is seen mainly to arise from T phonons generated very near the excitation surface. In addition, the observation that the phonon-wind force is stronger on an etched surface than on a polished surface indicates that the phonons generated in the damaged-layer-induced nonradiative-recombination processes probably do not play a significant role in the phonon-wind force. The dependence of the cloud parameters on the excitation photon energy seems to lie mainly in the resulting droplet distribution in the cloud rather than in the cloud extent.

C. Spatial anisotropy

The slit-scan data shown in Fig. 4 provide general information on the power and focus dependence of the EHD cloud *extent*. The slit-scan collection geometry, however, integrates over the

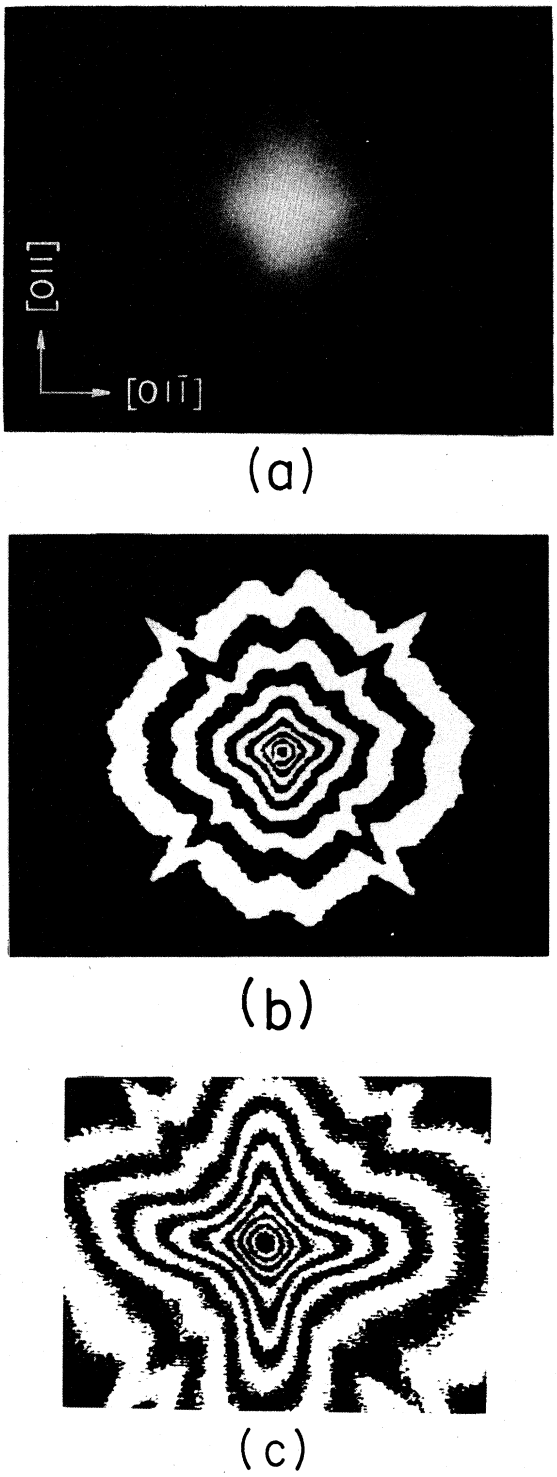

FIG. 7. Infrared image of the EHD cloud produced by focused excitation on a (100) etched surface, and viewed through the ($\bar{1}$00) surface. The photo width is $\Delta x = 2.5$ mm, $P_{inc} = 76$ mW. (a) Image as displayed on a storage oscilloscope. (b) Contour map; the alternating black and white bands connect contours of constant intensity. (c) Contour map of the central region of the cloud, $\Delta x = 1$ mm.

slit height, and hence loses spatial information. By using instead, an aperture, a two-dimensional image can be collected and the *spatial structure* of the cloud may be examined in detail.

Figure 7(a) is an infrared image[33] of an EHD cloud in Ge obtained by the imaging method described in Sec. II. Here, the laser strikes an etched (100) surface, and the cloud is viewed through the opposite ($\bar{1}00$) face. Thus, the image in this figure is a two-dimensional *projection* of the three-dimensional anisotropic EHD cloud. The cloud image displays a fourfold anisotropy with two prominent types of features: broad "lobes" near the vertical and horizontal directions and sharper "flares" that form an X pattern. A more informative version of this image can be obtained with some computer processing. In Fig. 7(b) a contour map is constructed from the image in Fig. 7(a). The alternating black and white bands connect contours of constant intensity. The contour map, constructed from the digitized image, allows an examination of the cloud shape over a much greater dynamic range of intensities, revealing an evolution of the cloud shape with radial distance from the central excitation point.

Figure 7(c) shows a magnified view of the central cloud region. At the center, the circular contours are determined by the laser spot size. At slightly larger radial distances, the four lobes are most prominent. As we will show below, these central lobes are actually along the ⟨111⟩ crystalline directions. At further distances, the lobes become less prominent and the flares start to appear. On either side of the flare a region of slightly lower intensity is observed; this region appears to be partially depleted of EHD. It can also be seen that at large radii the lobes are split. These general anisotropic features of the cloud are now well accounted for by an anisotropic-phonon-wind model.[11,17,34] Before describing the feature of this theory in detail, we proceed to enumerate further properties of the EHD cloud in Ge.

To determine the true three-dimensional structure of the cloud, views from other orientations are required. To examine the penetration of the cloud into the crystal and the orientation of the broad lobes, the cloud can be imaged from the side, looking along the excitation surface and perpendicular to the [100] excitation axis. In Fig. 8 two such side views are presented. The vertical lines at the left are the excitation surfaces seen edge on. When the cloud is viewed along [010], as in Fig. 8(a), a single sharp flare is observed and the lobes form an angle of 90°. Together with Fig. 7, this implies that the broad lobes point along the ⟨111⟩ axes. In Fig. 8(b) the cloud is imaged along [011]. This is a different crystal with (011)

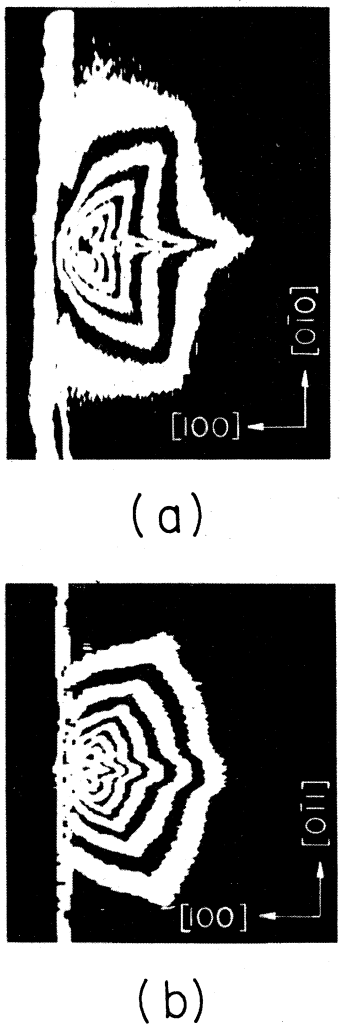

FIG. 8. Side view of the [100] pumped cloud $P_{inc} = 76$ mW. The laser excites the crystal from the left. The vertical line is the excitation surface. (a) Viewed along [001], $\Delta x = 5.4$ mm. (b) Viewed along [011], $\Delta x = 6.5$ mm.

faces cut perpendicular to the (100) excitation face; therefore, one can imagine Fig. 8(a) as rotated 45° about the excitation axis. A broader flare, normal to the surface, is observed and the lobes now form an angle of about 109° as expected for two ⟨111⟩ axes viewed along [011]. In this view the apparent broad flare is actually a superposition of a flare and the other two ⟨111⟩ lobes.

This pair of images confirms that the lobes are indeed along the ⟨111⟩ axes, and further suggests that two types of sharp-flare structures exist. This latter point will be discussed in detail in Sec. III D. For the present, we note that there exists a set of sharp {100} planar flares and a somewhat broader set of ⟨100⟩ axial flares. In Figs. 7 and

8(a) the planar flares are observed edge on, and in Fig. 8(b) the axial flare is observed. This axial flare is of course present in both Figs. 5 and 8(a); it is superimposed with the other intensities. Close examination of Fig. 8 also confirms that the region of maximum EHD intensity is indeed inside the crystal as indicated in Figs. 4(a) and 4(c).

As might be expected, the anisotropic structure of the droplet cloud is most pronounced at high excitation levels. At very low levels the cloud size approaches that of the excitation spot. In fact, the spatial anisotropy of the cloud is only observed at incident powers above several hundred microwatts. The power dependence of the cloud shape is illustrated in Fig. 9. As can be seen in Fig. 9(a), at an intermediate power of 7.6 mW, both the central lobe structure and the flares are not as well pronounced. At lower power, Fig. 9(b), the cloud tends to lose its sharp anisotropies, and the angular width of the flares approaches that of the lobes. Clearly, Fig. 9(b) does not scale up to Fig. 7(b).

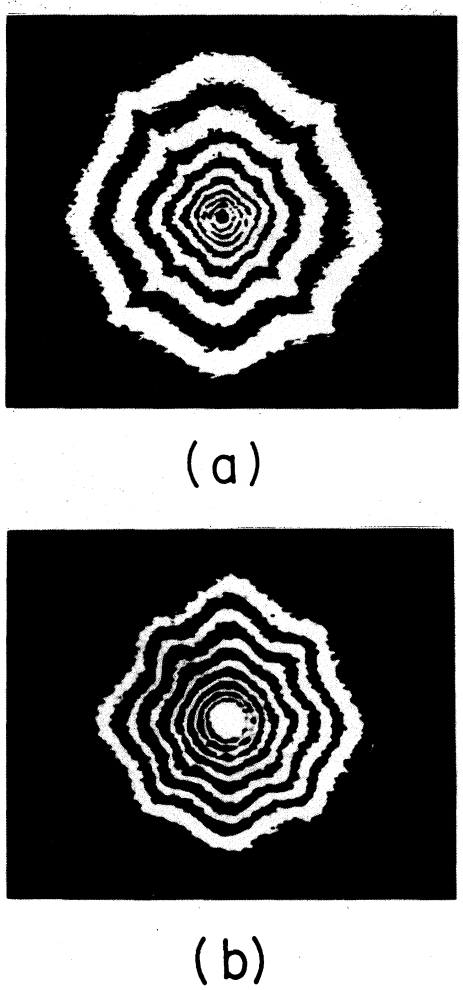

FIG. 9. Power dependence of the cloud shape for focused excitation on an etched (100) surface. (a) $P_{\text{inc}} = 7.6$ mW, $\Delta x = 2.5$ mm. (b) $P_{\text{inc}} = 2.3$ mW, $\Delta x = 2.0$ mm.

This reduction in the anisotropy at intermediate laser powers, 1–50 mW, cannot be completely explained by the finite laser spot size. The circular shaped contours in the interior of Fig. 9(b) extend to about 0.5 mm, which is considerably larger than the 100-μm spot size. Also, this smaller cloud does not resemble the interior of the larger clouds, as expanded in Fig. 7(c). Something fundamental to the anisotropy seems to be changing with excitation power. We suggest two possible explanations for this effect. The first involves a change in the energy distribution of the ballistic phonon flux with excitation power. In Sec. IV we will approximate this unknown distribution function as a Planck distribution at an elevated temperature T_p. As we will show, the anisotropy of the phonon-wind force has a distinct dependence on the parameter T_p. It remains to be shown, however, whether the laser power density affects T_p. Secondly, the reduced anisotropy at low powers may represent an increased role of the diffuse R phonons. To a first approximation, the average cloud density is independent of excitation power, and thus the net flux of R phonons at a given point inside the cloud is constant. On the other hand, the T-phonon flux at this point depends directly on excitation level. Thus at lower powers the R phonons at a fixed radius should become relatively more important, producing a more isotropic cloud.

The anisotropic cloud shape is, of course, strongly dependent on the size of the excitation region, i.e., the size of the T-phonon source. In Fig. 4(c), the dependence of the EHD penetration depth upon focus was shown. As the cloud flattens against the surface it also loses it anisotropic shape, as shown in Fig. 10. For a laser spot size of about 300 μm, Fig. 10a, the flares have almost disappeared and the prominence of the lobes is actually enhanced. For an excitation region of about 500 mm, Fig. 10(b), the cloud is diamond shaped. Further defocusing produces a cloud with circular contours. In summary, the sharp-flare structure is quite sensitive to the focus condition, while the broad lobe structure is less sensitive.

The cloud images presented thus far have all been produced with (100) excitation surfaces. By exciting other crystal surfaces the full symmetry of the EHD cloud may be observed, and the full three-dimensional nature of the cloud can be illustrated. The threefold symmetry of a $\langle 111 \rangle$ view of the cloud is shown in Fig. 11(a). Here the sample is pumped on a (111) face and imaged through the opposite face. Three lobes are observed; a fourth lobe, along the viewing direction, contri-

butes luminescence intensity to the center of the image. Three flares are also observed. These are the axial ⟨100⟩ flares.[35] It is interesting to note that the interior contours, nearest the excitation point, do not push out towards the ⟨111⟩ directions as in Figs. 7(b) and 7(c); instead, they are oriented toward the ⟨100⟩ axial flares. We believe that this formation is due to a topological feature in the slow TA phonon focusing near the ⟨111⟩ directions as will be discussed in Sec. IV.

A side view with laser excitation on a (110) face, as viewed along [001], is presented in Fig. 11(b). Two flares are evident, each a superposition of the two types of flares. The observed broad lobe is actually the superposition of the two lobes, one directly behind the other. This image corresponds to the slit-scan data of Fig. 4, and was chosen for that experiment in order to minimize the effects of cloud anisotropy on the shape of the slit-scan traces. It clearly reveals that the flares originate at the excitation point, not at the point of maximum EHD intensity, located well inside the crystal. It follows that the phonons responsible for this sharp cloud structure arise from the excitation region, not from the droplets themselves.

D. Flare structure

The planar nature of the flares observed in Fig. 7 can be demonstrated with a straightforward rotation experiment. The basic idea is simple: rotate the sample so that the flares are observed at a slightly oblique angle. A planar structure will

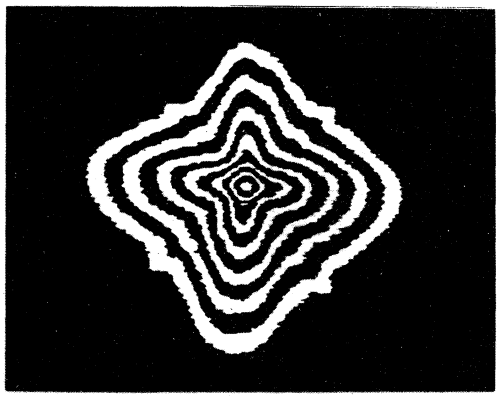

(a)

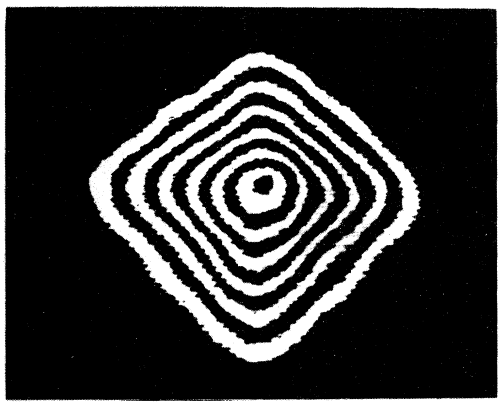

(b)

FIG. 10. Focus dependence of the cloud shape. P_{inc} = 76 mW as in Fig. 7, Δx = 2.3 mm. (a) Laser spot diameter = 300 μm. (b) Laser spot diameter = 500 μm.

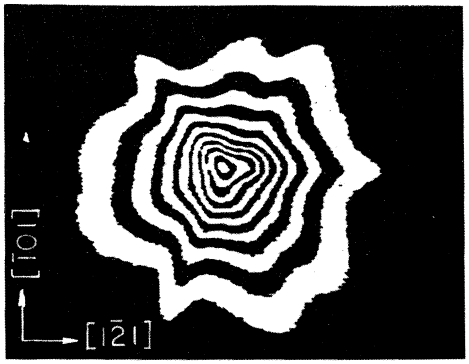

(a)

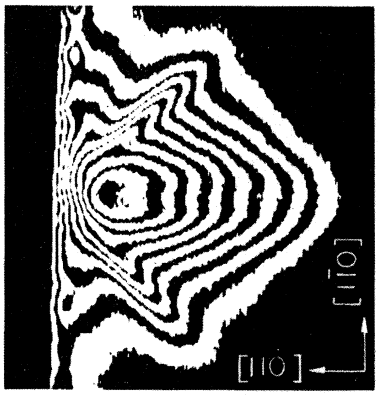

(b)

FIG. 11. (a) Excitation on a (111) surface, face view, Δx = 3.5 mm, P_{inc} = 76 mW. (b) Excitation on a polished surface (110), [001] viewing direction. The laser strikes the crystal at the left. This image corresponds to the excitation geometry for the slit-scan data in Fig. 4; Δx = 1.6 mm, P_{inc} = 15 mW.

then appear to lose its sharpness while an axial structure will remain sharp. The sample is initially viewed normal to the $(\bar{1}00)$ face and excited on the (100) face. The [001] axis is vertical, so the pattern is similar to Fig. 7, but rotated 45° about the viewing axis. The sample is then rotated 20° about the vertical [001] axis, and the resulting image is presented in Fig. 12. The vertical flares are greatly reduced while the horizontal flares remain unperturbed. This implies that the sharp flares are mainly due to a concentration of electron-hole droplets in the {100} planes of the crystal. The result cannot be explained by a set of axial ⟨100⟩ flares.[36]

Recent phonon-focusing work in Ge has predicted[37-41] and observed[38,40-42] singularities in the flux of TA phonons emanating from a point heat source. Specifically the fast TA (FTA) mode is channeled into a ridge within ± 2° of the {100} planes, and the slow TA (STA) mode is mostly channeled into an approximately square pattern 15° on a side about the ⟨100⟩ axes (see Fig. 19). To identify the source of the flares, their angular width can be compared to that of the singularities in the phonon-flux distribution, as described below. A preliminary comparison of phonon-flux singularities and EHD cloud anisotropy was given by Wolfe *et al.*[43]

In all of the contour maps presented so far, the flares appear to have sharp ends. This is, however, merely an artifact of the image display technique. The flares actually have an approximately constant *angular* full width. This important point is illustrated in Fig. 13. A face view image of (100) excitation viewed through $(\bar{1}00)$ is presented as a hidden-line drawing in Fig. 13(a). This drawing is constructed by plotting, on an x-y recorder, the luminescence intensity along a subset of the horizontal scan lines of an image. The excitation point, near $x = 2.0$ mm and $y = 3.7$ mm, is positioned in order to clearly show the development of the flare. It can now be seen that as the flare recedes from the excitation point it broadens and decreases in amplitude. A dip in the intensity is observed on each side of the flare; these are the regions partially depleted of droplets. [This effect is observed as a notch in the contour maps, see Figs. 7(b) and 7(c).]

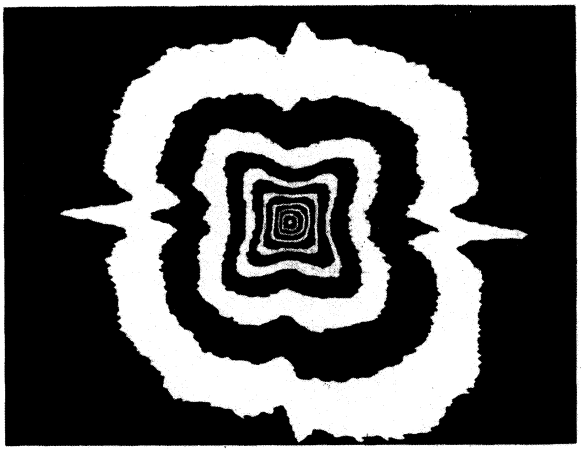

FIG. 12. Rotation experiment. Sample was rotated 20° about the [001] (vertical) axis. $P_{inc} = 228$ mW, $\Delta x = 2.5$ mm.

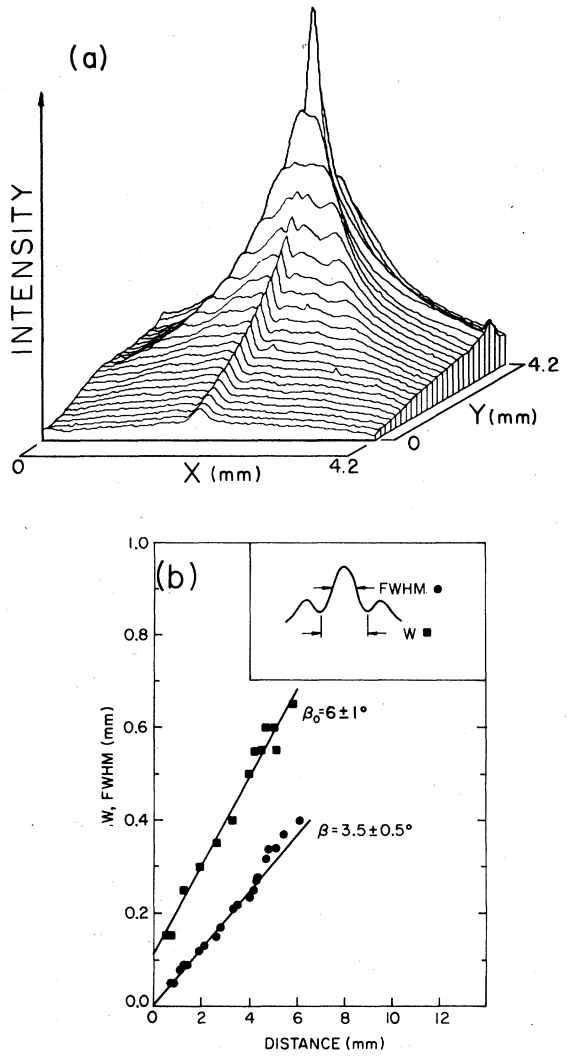

FIG. 13. Angular width of the flare structure. (a) Line drawing of a face view (100) excitation cloud image, oriented to display the nature of the flare. The flare is seen to broaden and decrease in amplitude as a function of distance from the cloud center. (b) Plot of the notch width, W, and the full width at half maximum, FWHM (defined in the inset), as a function of distance from the center of the cloud. Data from an image similar to and corresponding to the flares seen in Fig. 7.

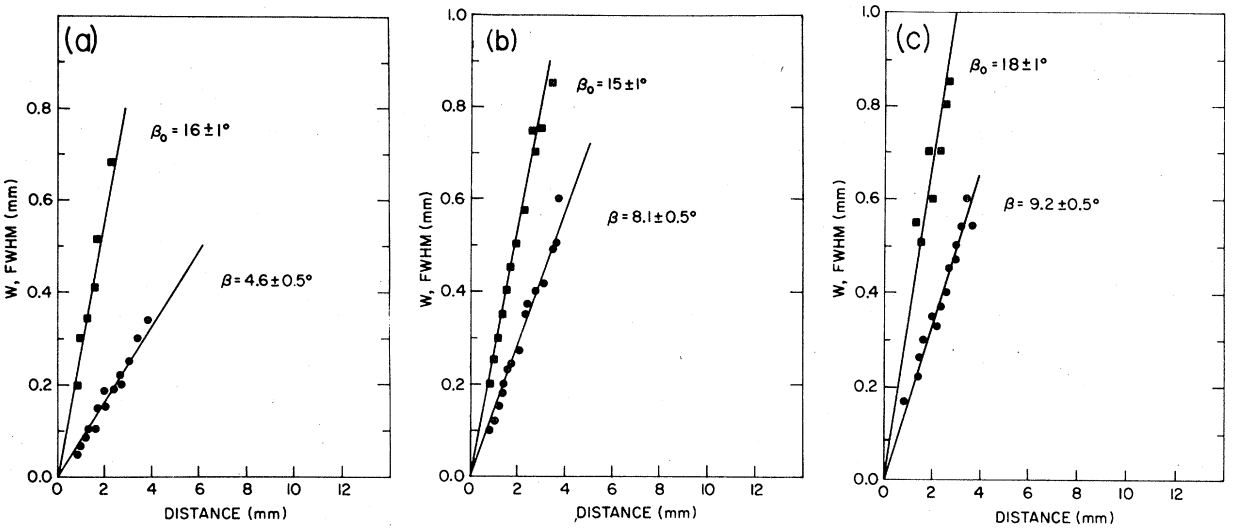

FIG. 14. (a) Angular width plot for the flares seen in a ⟨111⟩ view, such as Fig. 11(a). (b) Plot for the sharp flare seen in Fig. 8(a). (c) Plot for the broad flare seen in Fig. 8(b).

The flare structure is examined more quantitatively in Fig. 13(b) where the notchwidth (W) and the full width at half maximum (FWHM) of the flare structure, defined in the inset, are plotted as a function of distance from the center of the cloud. The observed linear relation indicates a constant angular width for both W and FWHM. These two angular widths are labeled as β_0 and β, respectively. A similar angular full-width plot can be made for the (111) excitation, as shown in Fig. 14(a). Both β_0 and β are much broader here. Finally, for completeness, the flare structures from side-view images like Fig. 8 are plotted in Figs. 14(b) and 14(c) to determine the values of β_0 and β for these cases.

In Table III these experimental values are compared to the calculated angular widths of the phonon singularities (which will be discussed in detail in Sec. IV). The term β_0' is the angular width of the singular region projected onto the viewing plane for comparison to the experimental values of β_0. The flare structures can now be identified unequivocally with specific TA-phonon modes. The planar flare structure is due to the planar distribution of the FTA mode in the {100} planes. The observed axial flare structure is due to the axial distribution of the STA mode in the ⟨100⟩ directions.

Two important facts can be learned from Table III: (1) The observed values of β_0 compare quite well with the properly projected values of the angular width of the singularities in the phonon flux β_0'. This implies that the regions partially depleted of droplets are precisely those of the phonon singularities. (2) The value of β is always less than β_0'. This implies that the EHD are channeled into a region of angular width smaller than the phonon singularities. This last observation is important evidence for the nonradial nature of the phonon-wind force, and gives the basic physical idea behind the formation of the flares. Droplets are swept out of the path of the intense TA-phonon flux, and channeled into regions of angular width smaller than the phonon-flux distribution. We return to this point in Sec. IV.

E. EHD and FE distributions at 4.2 K

The degree of anisotropy of the cloud has a distinct temperature dependence. At 4.2 K the cloud retains only a slight diamond shape as illustrated in Fig. 15(a). Although this image was produced with the same laser focus as Fig. 7, the

TABLE III. Comparison of the observed angular widths of the flare structure and the calculated phonon-flux singularities. The terms β and β_0 are defined in Fig. 14(b). The term β_0' is the angular width of the singular region projected onto the viewing plane.

Pump	View	EHD cloud β ±0.5	EHD cloud β_0 ±1.0	Phonons FTA β_0	Phonons FTA β_0'	Phonons STA β_0	Phonons STA β_0'
[100]	[$\bar{1}$00]	3.5	6	4.0	5.6	15	15
[100]	[010]	4.6	16	4.0	5.6	19.2	19.2
[100]	[011]	8.1	15			15	15
[111]	[$\bar{1}\bar{1}\bar{1}$]	9.2	18			15	18.2

anisotropy is almost gone. The reduced anisotropy is also accompanied by a somewhat increased average cloud density. This suggests that the effect is due to a reduction of the mean free path of the T phonons in the cloud at higher temperatures.

For comparison, an image of the free-exciton (FE) phase also at 4.2 K is shown in Fig. 15(b). This is accomplished by setting the spectrometer to the LA replica of the FE luminescence shown in Fig. 2. The free-excitons, being light-diffusive particles, exhibit an exponential-diffusion profile at sufficient distances into the crystal. The phonon-wind interaction appears to be weaker than diffusion. Unlike the EHD contour maps which tend toward small tight contours at the center, indicating a large intensity gradient, the FE image has broad contours near the center. This is because in this experiment at moderate excitation and 4.2 K, both EHD and FE coexist. Although this figure is spectrally resolved, the influence of the EHD is still present. Near the center of the distribution, the FE density is constrained by the presence of droplets. Beyond the edge of the EHD cloud an exponential profile is observed with a 1.5-mm diffusion length.

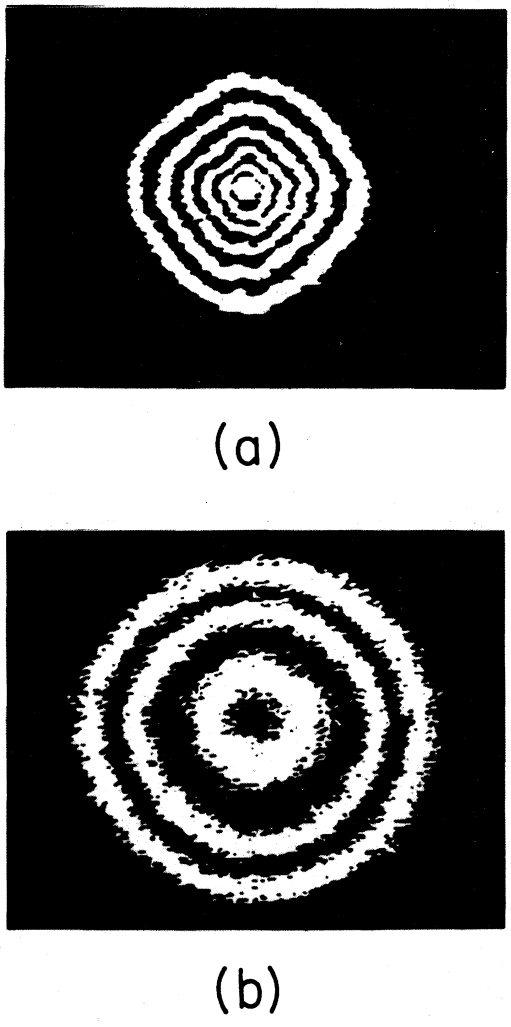

FIG. 15. 4.2 K data. (a) Spectrally resolved EHD image at $T=4.2$ K, $\Delta x=3.2$ mm, $P_{\rm inc}=23$ mW. (b) Spectrally resolved FE image at $\lambda=1.738$ μm and $T=4.2$ K. $\Delta x=5.0$ mm, $P_{\rm inc}=57$ mW.

IV. PHONON-WIND-FORCE CALCULATIONS

A. Introduction

The observation of the highly anisotropic EHD cloud[16] has provided the impetus to extend the basic phonon-wind ideas of Keldysh to include the proper anisotropy factors. Anisotropy enters this problem in two ways: (1) from the anisotropic energy flux of ballistic phonons emanating from a point source; i.e., phonon focusing, and (2) from the electron-phonon interaction which depends upon both the deformation potential matrix element, and the ellipsoidal electron Fermi surface. This interaction is calculated in $\vec{q}$ space, and, therefore, its relation to the observable real-space anisotropy depends on the angular relation between $\vec{q}$ and the phonon group velocity $\vec{V}$. If $\vec{q}$ and $\vec{V}$ were always collinear (as is almost the case for the LA mode), then $\vec{q}$-space anisotropies would be directly reproduced in real space. However, for the two TA modes $\vec{q}$ and $\vec{V}$ are rarely collinear, and the transformation from $\vec{q}$ to real space is quite complex. Therefore, the phonon-wind force is first calculated as a function of $\hat{q}$ and then transformed into $\hat{r}$.

As mentioned in Sec. I, the basic idea of the phonon wind is that the absorption of a flux of ballistic phonons, by carriers within a droplet, produces a net momentum transfer along $\hbar\vec{q}$. The calculation of the force basically entails a calculation of the absorption rate. Once the anisotropic force is calculated, Eqs. (5) and (6) provide a convenient link to the observable density profile of the droplet cloud. Actually, Eq. (5) is the solution to the continuity equation, Eq. (4), for radial forces only. A solution to Eq. (4) for a nonradial force is much more complicated, and at this point has not been accomplished. For the nonradial phonon-wind force, the solution to Eq. (4) is no longer analytical. However, for most angles, $\vec{q}$ and $\vec{V}$ are within 10° of each other, and we therefore regard the use of Eq. (5), with $\lambda=\lambda(\theta,\phi)$, as a good first approximation in calculating the cloud density.

In this theory section we present a set of calculations of the various components of the phonon-wind force associated with a localized source of heat. In Sec. IV B the expression for the anisotropic

force, given first by Markiewicz,[17] is discussed and constant cloud density calculations from this expression are reviewed. In Sec. IV C the different contributions to this anisotropy are examined, and brought together in Sec. IV D to calculate the phonon-wind force. Finally, in Sec. IV E the nonradial nature of the phonon-wind force is displayed by calculating droplet trajectories.

B. Markiewicz's expression for the force

Markiewicz[17] took the variational calculation[44] for the lattice contribution to the electrical resistivity in a metal as a model for the calculation of the phonon-wind force. The common link here is that both the resistivity and the force [see Eq. (1)] involve essentially a calculation of τ_p, the momentum damping time for a carrier. The force per e-h pair $\vec{F}(\vec{r})$, on a droplet at position $\vec{r}$ from the excitation point, is the phonon momentum $\hbar\vec{q}$ times the absorption rate integrated over all carrier momenta and phonon energies. The coupling between a phonon with lattice displacement $\vec{u} = \hat{e}u\exp[i(\vec{q}\cdot\vec{r} - \omega t)]$ and a carrier is described by a deformation-potential matrix element $(\vec{q}\cdot\vec{D}\cdot\hat{e})$, where $\vec{D}$ is the deformation potential tensor and $\hat{e}$ is the polarization of the elastic wave. Markiewicz's complete expression for the phonon-wind force is

$$\vec{F}(\vec{r}) = \frac{-\pi}{2\rho n_0}\sum_{\alpha}^{3}\sum_{i}^{5}\int\frac{d^3k}{(2\pi)^3}\int\frac{d^3q}{(2\pi)^3}\hbar\vec{q}\,\frac{(\vec{q}\cdot\vec{D}\cdot\hat{e})^2}{\omega_\alpha} \times N_q^*(\vec{r})f(E)[1-f(E_1)] \times \delta(E_1 - E - h\omega_\alpha), \quad (8)$$

where the integrals are over the electron (k) and phonon (q) states, and the result is summed over the three phonon modes ($\alpha = 0$, 1, and 2 = LA, STA, and FTA) and the five effective carrier species (electrons in the four ⟨111⟩ valleys and the holes). The nonequilibrium phonon distribution is described by N_q^*. The electron Fermi distribution functions are $f(E)$, and $\delta(E_1 - E - h\omega_\alpha)$ is the energy-conserving delta function, with E and E_1 the initial and final electron energies in the scattering event. The crystal density is ρ, and n_0 is the electron-hole liquid density. In Sec. IV C we will discuss the various components of Eq. (8).

In order to evaluate this expression for the force, the nonequilibrium phonon distribution function is required. In Ref. 17, Markiewicz assumed this unknown distribution function could be approximated with an equilibrium Planck distribution at an elevated temperature T_p above the lattice temperature T. The nonequilibrium phonon distribution, at a distance $\vec{r}$ from a localized source is then assumed to be

$$N_q^*(\vec{r}) = C_\alpha(r_0/r)^2 N_q(T_p)A_\alpha(\hat{r}), \quad (9)$$

with $N_q(T_p)$ the Planck distribution. Here C_α is a normalization constant for the number of phonons produced, $(r_0/r)^2$ is the inverse-square-law dependence of the force due to the geometric reduction of the phonon flux with distance from a point source, and $A(\hat{r})$ is the phonon-flux enhancement term that contains the angular dependence of the ballistic phonon flux. We can now see that the electron-phonon-coupling anisotropy is contained in the term $(\vec{q}\cdot\vec{D}\cdot\hat{e})^2/\omega_\alpha$, while the phonon-flux anisotropy is contained in the term $A(\hat{r})$.

This calculation for the force contains several important assumptions: (a) The Planck distribution is used in N_q^*. This is the simplest reasonable approximation and gives us a single parameter T_p to characterize the nonthermal phonon-energy distribution. In Refs. 11 and 34 an attempt was made to calculate the actual phonon distribution resulting from phonon emission by hot carriers. (b) The source of phonons is assumed to be localized. This amounts to neglecting the R-phonon contribution and assuming T phonons are created within a volume of characteristic dimension r_0 near the excitation point. (c) The density of droplets on the surface of this volume is assumed to be constant. The physical meaning of this assumption is discussed in Sec. V. In this calculation the volume is taken for convenience as $\frac{2}{3}\pi r_0^3$, a hemisphere. (d) The force is assumed to have an inverse-square-law dependence. Phonon-focusing effects will modify this r^{-2} dependence near the phonon singularities,[45] however, this deviation will be neglected here.

Markiewicz made these approximations, took the statistical tabulation of $A(\hat{r})$ by Taylor, Maris, and Elbaum,[38] and calculated the anisotropic-phonon-wind force. In this calculation the STA mode was assumed to occupy a circular cone of half-angle 7.5° about the ⟨100⟩ axes, and the FTA mode was assumed to be concentrated into a ridge within a constant 4° width about the {100} planes. With this calculated force, Eqs. (5)–(9) were used to construct constant-density surfaces for the clouds. Using Eqs. (6) and (7), the radius R to a constant-density surface is defined by $R = BF^{1/3}$, where $F(\theta, \phi)$ is evaluated at a constant distance from the excitation point, and B is a constant.

Figure 16 reproduces[46] these three-dimensional constant cloud density contours. The three figures correspond to three different constant-density levels. In this calculation *radial* phonon-wind forces were used with the exception of the regions near the ⟨100⟩ axes, where large deviations are known to occur. In these regions a two-dimensional diffusion equation was used to approximate

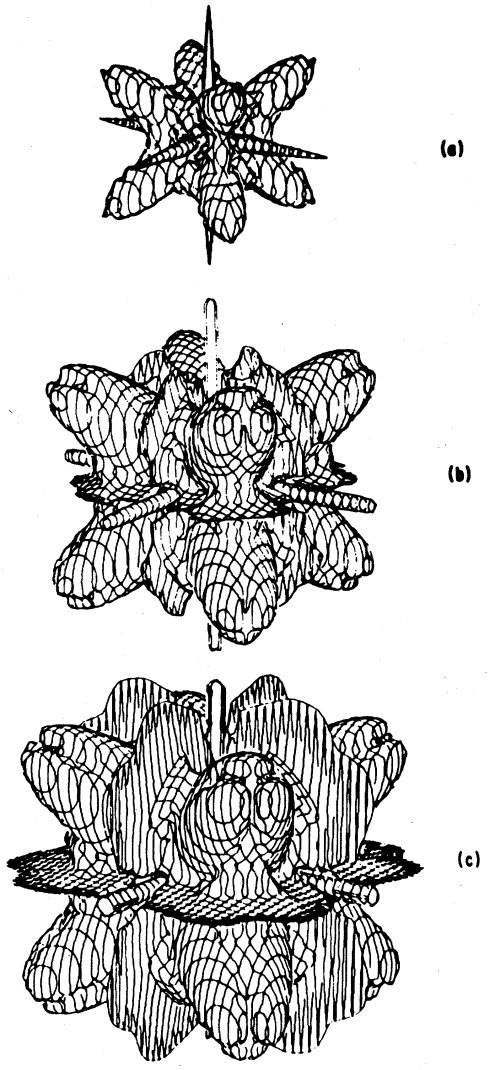

FIG. 16. Theoretical constant cloud density contours at three density levels for the cloud. This calculation includes the effects of nonradial EHD velocities near the ⟨100⟩ axes. In the bottom two figures the ⟨100⟩ flares are truncated for clarity.

the effect of the nonradial phonon-wind force. A finite absorption length for the LA mode was also incorporated, predicting the change over from an LA-dominated force in the central region of the cloud (top) to a TA-dominated force at larger radial distances (bottom).

To compare this calculated constant-density surface to the experimental contour maps, a sum of the three-dimensional density $n(\vec{r})$, along the viewing direction was first calculated. A contour map of the two-dimensional projection of the cloud is then constructed. The resulting calculated contour map[46] is shown in Fig. 17. This calculation

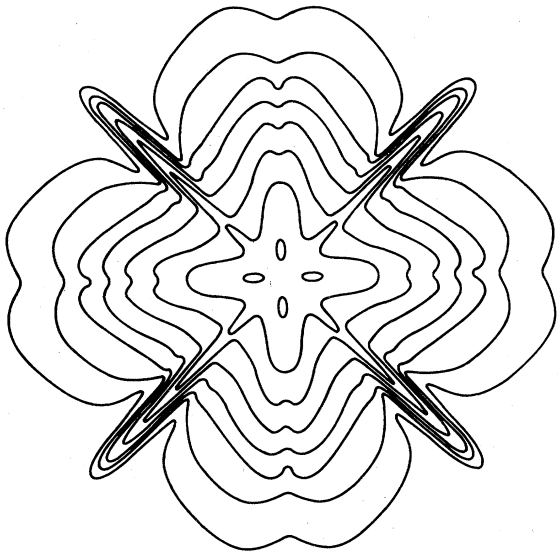

FIG. 17. Calculated contour map of droplet densities projected into the (100) plane, to be compared with Fig. 7(b).

compares quite well with the observed contour map, see Fig. 7(b). Both the evolution of the cloud shape with the distance from the excitation point and the detailed flare structure are reproduced. This calculation of Markiewicz's provides a very graphic and global picture of the anisotropic droplet distribution due to the phonon-wind force. In addition, Eq. (8) provides the starting point for the detailed calculations described in the rest of this section.

C. Anisotropy factors

A great deal of physical insight may be obtained by examining individually each of the contributions to the total anisotropic-phonon-wind force. These contributing factors are (1) the anisotropic flux of ballistic phonons from a point source, (2) the deformation-potential matrix element, (3) the ellipsoidal electron Fermi surface, and (4) the nonequilibrium phonon-energy distribution characterized by the temperature T_p. The discussion of the T_p dependence will be deferred until Sec. IV D where the functional form of the dependence is obtained.

1. Phonon-flux distribution $A(\hat{r})$

Both experimental[16,18] and theoretical[11,17] work demonstrate that thermalization phonons, emanating from a localized source at the excitation region, play a dominant role in the phonon-wind force. In this section we concentrate on these phonons. It has rather recently become appreciated that

acoustic phonons propagating ballistically from a localized heat source exhibit a highly anisotropic energy flux, even in a cubic crystal such as Ge. This angle-dependent flux is a simple consequence of the elastic anisotropy of the crystal, and is referred to as phonon focusing.[37,38]

The flux of ballistic phonons (energy flux) occurs along the group velocity direction defined as $\vec{V}_\alpha = \partial\omega_\alpha(\vec{q})/\partial\vec{q}$. As noted above, the momentum transfer (impulse) is along the direction of the phonon momentum $\hbar\vec{q}$. In an anisotropic crystal such as Ge, $\vec{q}$ and $\vec{V}$ are in general *not* collinear. This is the origin of nonradial nature of the phonon-wind force, and is also a central concept for the discussion in this section.

The basic ideas of phonon focusing are illustrated in Fig. 18(a), which shows an actual constant-frequency surface $\omega_\alpha(\vec{q})=\omega_0$, in the $(1\bar{1}0)$ plane for the LA mode using the known elastic constants[47] of Ge. The group velocity $\vec{V}$ is normal to the constant-ω surface, as shown. Since this surface is defined by $|\vec{q}|=\omega_0/v$, the deviation from sphericity implies an angular variation in the phase velocity of the elastic wave. The constant-ω surface is also called the "slowness surface".

Deviations from a spherical slowness surface, due to the elastic anisotropy of the crystal, produce a concentration or focusing of group velocity vectors along certain directions. This produces an enhancement of the energy flux along these directions. The enhancement factor A, compared to a hypothetical isotropic solid, can be calculated from the known elastic tensor[47] of Ge, and is defined[37] as

$$A=\left|\frac{\Delta\Omega_q}{\Delta\Omega_r}\right|, \tag{10}$$

where $\Delta\Omega_q$ and $\Delta\Omega_r$ are corresponding solid angle segments in wave-vector and real space, respectively.[48] In the case of an "isotropic solid" this ratio is unity. The enhancement factor along a given $\vec{q}$ direction is inversely proportional to the (Gaussian) curvature of the slowness surface at that point.

For the enhancement factor Markiewicz used the tabulated statistical enhancement factors of Ref. 38. Using a recently developed method of Northrop and Wolfe,[40,41] we can now analytically calculate the exact enhancement factors for any propagation direction. In order to calculate $A(\hat{r})$ we must first calculate $A(\hat{q})$ and then use the relation between $\vec{q}$ and $\vec{V}$ to transform back to real space. Formally this means

$$A(\hat{r})=\int_0^{4\pi} d\Omega_q A(\hat{q})\delta(\hat{q}-\hat{r}), \tag{11}$$

where $\hat{r}$ is along $\hat{V}$, and the delta function $\delta(\hat{q}-\hat{r})$ is defined by $\int_0^{4\pi}d\Omega_q\delta(\hat{q}-\hat{r})=1$. This factor $A(\hat{r})$ is plotted, as a polar plot, in Fig. 18(b) for the LA mode in the $(1\bar{1}0)$ plane. A broad peak in the LA energy flux occurs near the [111] direction, where the slowness surface is flattest. Along this direction the enhancement factor is $10\times$ that along the [100] direction. This general trend was experimentally observed for Ge in the heat-pulse experiments of Hensel and Dynes.[42]

The two TA modes are much more complex; along certain directions $A(\hat{r})$ is actually singular in the context of the geometrical optics approximation.[45] These integrable singularities have been explained by a careful examination of the topology of the TA-phonon slowness surfaces,[40,41] and correspond to regions of zero Gaussian curvature on these surfaces. For the TA modes the group

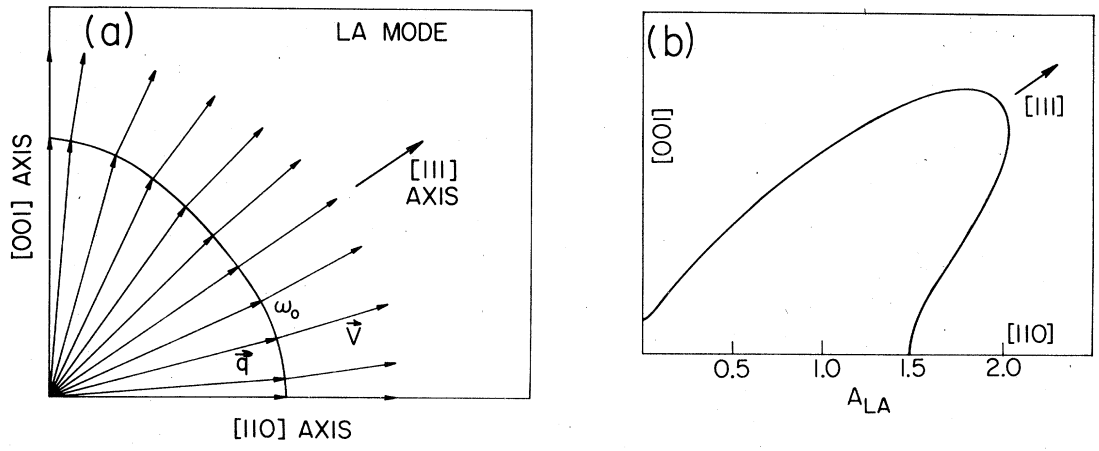

FIG. 18. Phonon focusing; the enhancement factor. (a) Calculated constant-frequency surface for the LA mode showing noncollinearity of $\vec{V}$ and $\vec{q}$ in $\vec{q}$ space. (b) Polar plot of the calculated enhancement factor for the LA mode in Ge plotted in the $(1\bar{1}0)$ plane.

velocity is often a multivalued function of $\hat{r}$. This means that for a given propagation direction more than one set of phonons will propagate. Each set will have a distinct $\vec{q}$ vector for the given group velocity direction $\hat{V}$. The singularities in $A(\hat{r})$ occur at folds of the multiple-valued group velocity surface where the number of sheets changes. These ideas are discussed in detail in Refs. 40 and 41.

In Ref. 39 Rösch and Weis displayed the phonon-intensity functions, proportional to $A(\hat{r})$, in a particularly instructive manner. Figure 19 is a reproduction of their polar plots, representing the ballistic phonon flux from a point source in Ge. Each phonon mode is displayed individually, and the normalized sum of the modes is displayed at the top left. The FTA mode is concentrated into a ridge within $\pm 2°$ of the $\{100\}$ planes. The STA mode is mostly concentrated into an approximately square pattern subtending ~15° centered on the $\langle 100 \rangle$ axes and an approximately triangular pattern subtending ~18° centered on the $\langle 111 \rangle$ axes. In these polar plots phonon intensities above 2.5 are truncated (black regions). We note here that a distributed phonon source, such as the R phonons, will not display these sharp features—they will be averaged out. Since sharp features corresponding to those of Fig. 19 are actually observed in the droplet cloud, it must be concluded that a localized phonon source provides the phonon-wind flux. A comparison of Figs. 16 and 19 clearly show that, for the two TA modes, $A(\hat{r})$ exerts a major influence on the phonon-wind force.

In the regions of high phonon-flux intensity there is actually a detailed fine structure, as shown

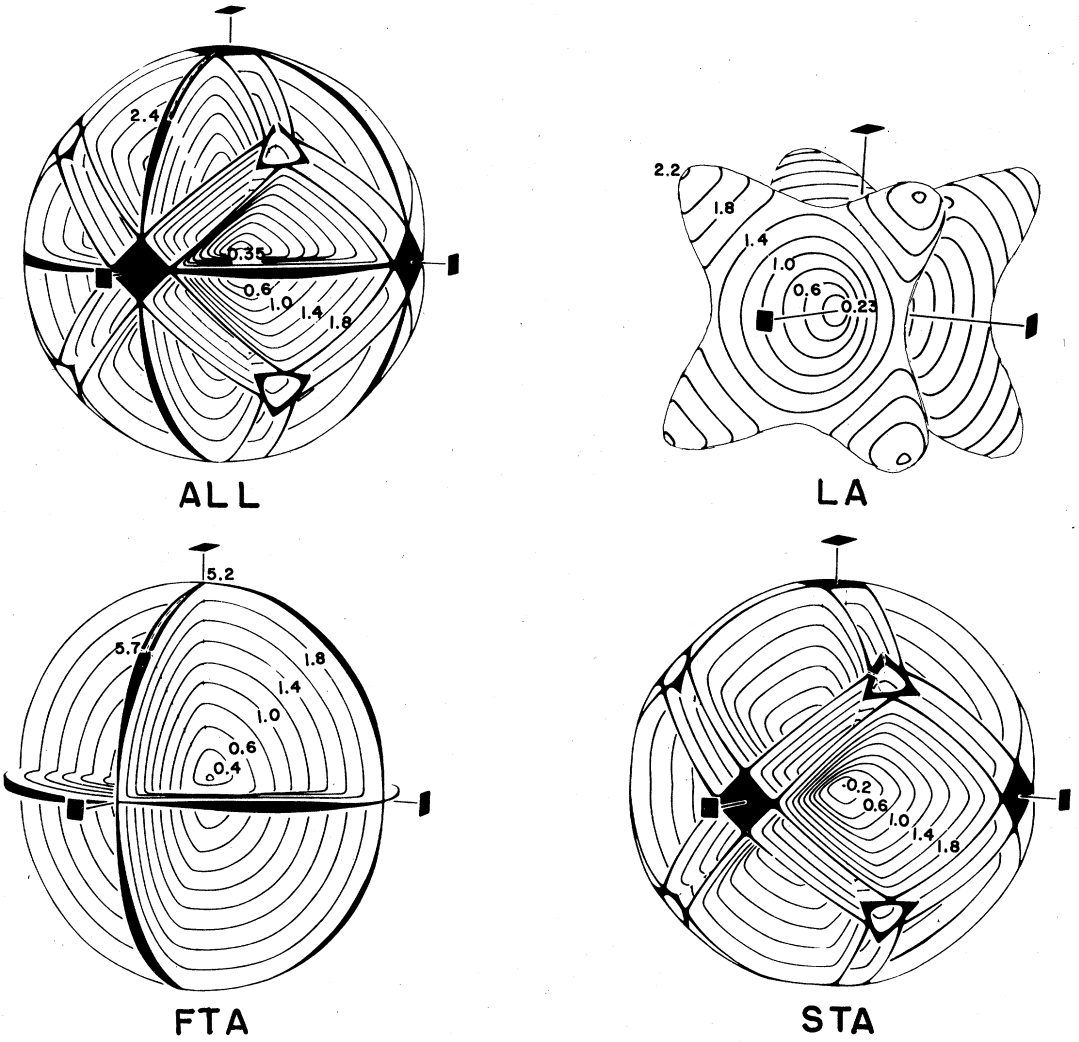

FIG. 19. Three-dimensional polar plots of the phonon-intensity surface for all three modes (from Ref. 39, with permission). At the top left the total intensity is given.

graphically by the ballistic phonon images in Refs. 40 and 41. To display this structure quantitatively, the enhancement factor from Eq. (11) is plotted in the $(1\bar{1}0)$ plane in Figs. 20(a)–20(c) for each of the three phonon modes. In order to display the wide range of the enhancement factor intensities, these are polar plots of the log of $A(\hat{r})$. This calculation is performed at 0.10° intervals in the plane, and, therefore, the relative height of the calculated spikes depends on their proximity to the exact location of the singularity. Thus, the absolute magnitude of the spikes is not particularly meaningful. In addition, in the actual cloud the singularities are integrated over finite solid angles producing a finite phonon flux.

In Fig. 20(b) no FTA phonons propagate between $\theta = 40°$ and 70°; this is the phenomenon of internal conical refraction about the ⟨111⟩ axes.[49] At $\theta = 88.1°$, the number of $\vec{q}$ vectors mapped into $\hat{V}$ jumps from 1 to 3, and $A(\hat{r})$ displays this discontinuity with a sharp jump in magnitude. The enhancement $A(\hat{r})$ for the STA mode is shown in Fig. 20(c). The spikes at 7.5° correspond to the edges of the black squares in Fig. 19. There is an additional enhancement spike inside this 15°-wide square. This structure was originally observed by Hensel and Dynes,[42] and it corresponds to the inner square observed in the ballistic phonon images of Northrop and Wolfe,[40] at 5.5° from the [001] axis in this plane. At the inner square the number of $\vec{q}$ vectors jumps from 9 to 7 as θ increases. At the outer square the number jumps from 7 to 3. The two sharp peaks near [111] correspond to the upper vertex and the lower side of the triangle seen in the STA plot of Rösch and Weiss, see Fig. 19. We believe that it is this triangle that is responsible for the central features of Fig. 11(a). A plot of $A(\vec{r})$ for all three modes in the $(0\bar{1}0)$ plane is given in Fig. 20(d). Note that in this plane, the FTA slowness surface is spherical and therefore A_{FTA} has a constant value. Thus, the flux of ballistic phonons emanating from a localized source is quite anisotropic and each phonon mode makes a unique and identifiable contribution to the total ballistic phonon-flux distribution.

The enhancement factor $A(\hat{r})$ such as plotted in Figs. 18–20 does not, however, contain all of the information required to compute the phonon-wind force. In addition to the phonon-flux intensities as a function of real-space direction, we also need the orientation of the associated phonon wave vectors. Again, we note that it is $\vec{q}$ that determines

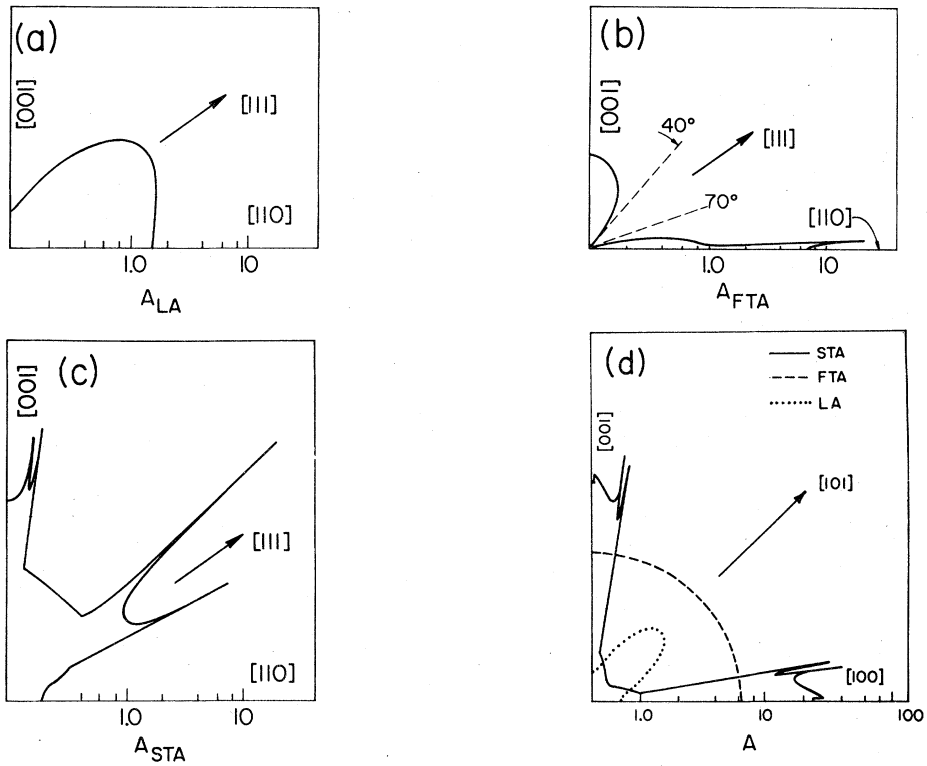

FIG. 20. Log polar plots of the enhancement factor $A(\hat{r})$ for each mode, calculated at 0.1° intervals. (a) LA mode in the $(1\bar{1}0)$ plane. (b) FTA mode, (c) STA mode, and (d) all three modes in the $(0\bar{1}0)$ plane.

the direction of the force. Figure 21(a) shows the calculated relationship between the direction of the wave vector $\vec{q}$ and that of the group velocity $\vec{V}$ for the FTA mode with $\vec{q}$ vectors in the $(1\bar{1}0)$ plane. The noncollinearity of $\vec{q}$ and $\vec{V}$ is evident. This noncollinearity cannot be divorced from $A(\hat{r})$; they are one and the same physical phenomenon. Again, internal conical refraction prevents propagation of the FTA mode in the vicinity of the $\langle 111\rangle$ directions. Near the location of the singularities, $\theta = 88.1°$ and $91.9°$, very small changes in the group velocity direction produce large changes in the direction of the associated wave vector. Indeed, as shown in Fig. 21(a), for the group velocity directions at the locations of the singularities, two very different wave vectors result. For those $\vec{V}$ directions between these two singularities the $\vec{q}$ vectors are oriented in towards the [110] axis. This is true for the FTA mode not only at the [110] direction, but throughout the (001) plane. (Recall from Fig. 19 that the FTA singularity structure is planar in nature.)

A similar plot for the STA mode is given in Fig. 21(b) for $\vec{q}$ vectors in the (001) plane. Within $\pm 9.6°$ from the [100] axis, at the angle of the phonon-flux singularity, the wave vectors are oriented in toward the [100] axis. This is the basic physical explanation for the observed flare structure: An intense flux of phonons along the singularities acts to channel droplets, in the case of the STA mode, toward the $\langle 100\rangle$ axes and, in the case of the FTA mode, toward the $\{100\}$ planes. The regions partially depleted of droplets in the experimental contour maps (the notches in the flare structures) appear to provide the experimental confirmation of this channeling effect.

It is also important to note that Fig. 21 does not display *all* of the $\vec{q}$ vectors associated with each $\vec{V}$. Only those wave vectors that lie in the given symmetry planes are shown. There are wave vectors outside of the symmetry planes which give rise to group velocity vectors in these planes. To calculate the force, *all* $\vec{q}$ vectors must be accounted for. This accounting is done formally with the integral in Eq. (11). In actual practice, a numerical two-dimensional root-finding scheme[50] is used to tabulate all of the $\vec{q}$'s associated with a given $\vec{V}$. This numerical method is required because of the multivalued nature of the group velocity.

2. *Deformation potential*

The phonon-wind force arises from the deformation-potential interaction between the nonthermal phonons and the carriers in the droplet. The interaction Hamiltonian takes the standard form[51]

$$H = \sum_{ij}^{3} D_{ij}\epsilon_{ij} , \tag{12}$$

where D_{ij} is the deformation-potential tensor and ϵ_{ij} is the strain tensor. For an indirect band-gap semiconductor, with nonspherical and degenerate conduction bands, the shift in the energy of the ith valley is generally written as[52]

$$\delta E_i = E_d \,\mathrm{Tr}\{\vec{\epsilon}\} + E_u\{\hat{a}_i \cdot \vec{\epsilon} \cdot \hat{a}_i\} , \tag{13}$$

with E_d, E_u the deformation-potential constants of Herring and Vogt,[53] $\hat{a}_i$ the unit vector along the ith $\langle 111\rangle$ conduction-band valley in Ge, and $\mathrm{Tr}\{\vec{\epsilon}\} = \epsilon_{xx} + \epsilon_{yy} + \epsilon_{zz}$, the dilation.

Equation (13) is a convenient form for δE when

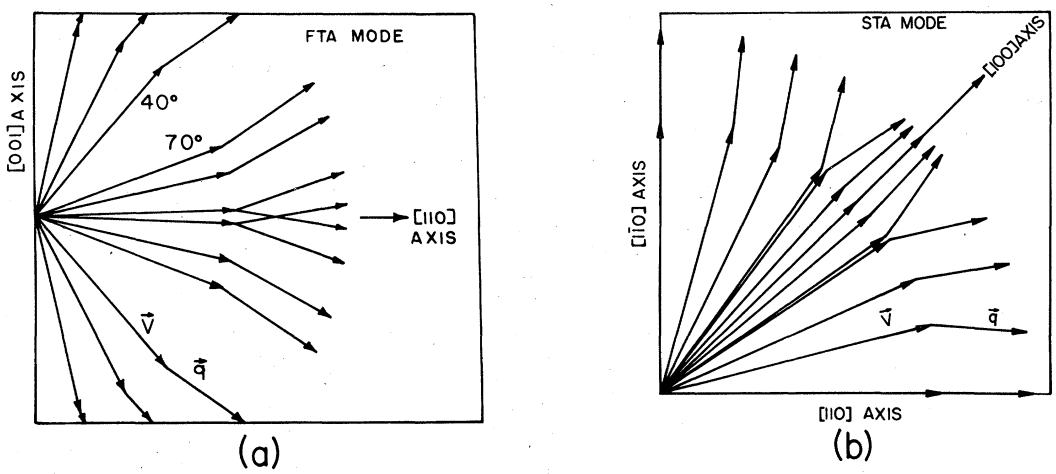

FIG. 21. Calculated angular relationship of $\vec{V}$ and $\vec{q}$ near the TA-phonon singularities. (a) For the fast TA mode with $\vec{q}$ in the $(1\bar{1}0)$ plane. Note that no $\vec{V}$ vectors propagate for $40° \leq \theta \leq 70°$, and $110° \leq \theta \leq 140°$, due to conical refraction near the $\langle 111\rangle$ directions. (b) For the slow TA mode with $\vec{q}$ in the (001) plane.

the static strain tensor $\vec{\epsilon}$ is known. However, for a dynamic strain associated with a phonon of wave vector $\vec{q}$ and polarization $\hat{e}(\hat{q})$ it is more convenient to convert Eq. (13) into the following form:

$$\delta E = \hat{q} \cdot \vec{D} \cdot \hat{e} . \tag{14}$$

In the present problem, phonons interact with the carriers in the droplet and, because of the high density $n_0 = 2.2 \times 10^{17}$ cm^{-3}, screening cannot be ignored. The electron and hole screened deformation-potential tensors[54] suggested by Markiewicz[17] were given as

$$\vec{D}_e = \left(E_{0e} + U_0 \frac{q^2}{q^2 + k_{\mathrm{TF}}^2} \right) \vec{I} + E_u \left(\hat{a}\hat{a} - \frac{\vec{I}}{3} \right) \tag{15}$$

and

$$\vec{D}_h = \left(E_{0h} - U_0 \frac{q^2}{q^2 + k_{\mathrm{TF}}^2} \right) \vec{I} . \tag{16}$$

Here $E_{0e} = -0.59$ eV, $E_{0h} = -8.31$ eV, $E_u = 19.3$ eV, $U_0 = 5.31$ eV, $k_{\mathrm{TF}} = 5.7 \times 10^6$ cm^{-1}, and $\vec{I}$ is the unit tensor. The screening is contained in U_0, the screening potential, and k_{TF}, the Thomas-Fermi (TF) screening length.

Figure 22(a) gives a polar plot in wave-vector space of the electron deformation-potential term summed over the four $\langle 111 \rangle$ conduction valleys for the LA mode with $\vec{q}$ in the $(1\bar{1}0)$ plane. For comparison the unscreened term is also plotted as the dashed line. The interaction is strongest for $\vec{q}$ along [111], and it can be seen that screening mostly reduces the interaction along [001]. The holes, taken as a spherical band, do not exhibit anisotropy in the deformation-potential term.

Figure 22(b) gives a similar polar plot for the two TA modes with $\vec{q}$ in the $(1\bar{1}0)$ plane. In this plane, along the [111] and [001] directions, the two TA modes have degenerate values. This is

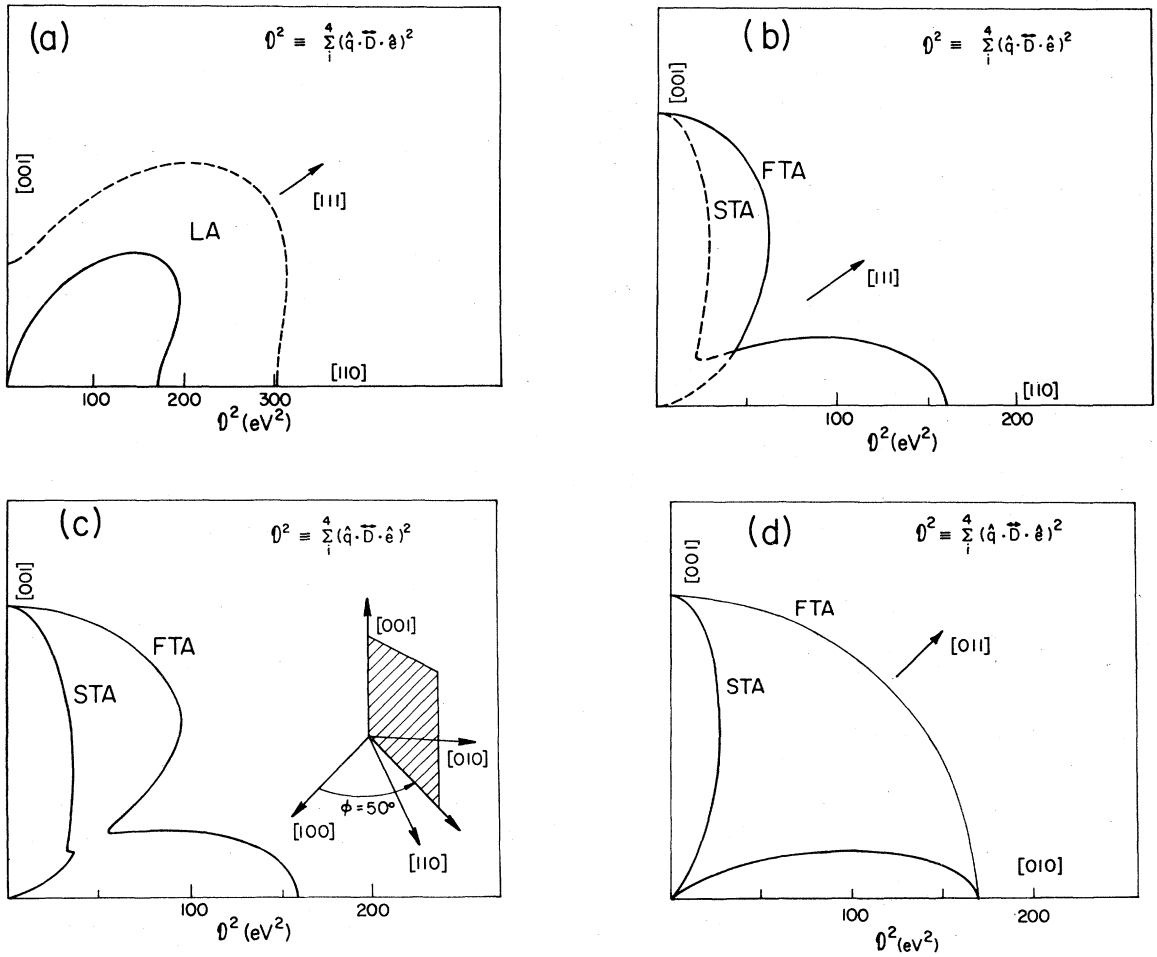

FIG. 22. Polar plots of the screened electron deformation-potential anisotropy factors as a function of $\hat{q}$. (a) LA mode; for comparison, the unscreened term is plotted as a dashed line. (b) TA modes; note that the modes are degenerate along [111] and [001]. (c) TA modes plotted in a plane 5° off of the $(1\bar{1}0)$ plane as shown in the inset. The degeneracy along [111] is now removed. (d) TA modes in the (100) plane.

a simple consequence of the fact that along these symmetry directions the two TA modes are degenerate solutions to the eigenvalue equation. The topology of the point of contact of the two *slowness* surfaces at the [111] is intimately related to the phenomenon of internal conical refraction.[49] The degeneracy along the [111] direction is removed out of the $(1\bar{1}0)$ symmetry plane as shown in Fig. 22(c). It is interesting to note that if only *one* valley, e.g., [111], is considered, the deformation potential is exactly zero for both TA modes when $\vec{q}$ is along the [111] axis. This is because, for a transverse mode with $\vec{q}$ along [111], $\hat{e}$ is in the (111) plane, and the ellipsoidal conduction valley is effectively spherical. The TA deformation-potential matrix element vanishes because $E_u = 0$ for a spherical valley[53] and $(\hat{q}\cdot\hat{I}\cdot\hat{e}) = 0$ for a pure transverse mode (i.e., $\hat{q}\cdot\hat{e} = 0$). Finally, for completeness, the TA deformation-potential terms are plotted in Fig. 22(d) for $\vec{q}$ in the (100) plane.

3. *Electron Fermi surface*

The momentum transfer involved in the phonon-wind force occurs via the absorption of a phonon of energy $\hbar\omega$ and momentum $\hbar\vec{q}$. Conservation of energy and momentum place constraints on those phonons suitable for the absorption process. As a degenerate Fermi system, the EHD absorb phonons by the scattering of carriers across the ellipsoidal Fermi surface. For a system in which $\hbar\omega \ll E_F$, and a given $\vec{q}$ direction, the absorption probability $P(q)$ is linear[51] in q up to a cutoff at the Fermi diameter $\vec{q} = 2\vec{k}_F$.

To explain the linear dependence of $P(q)$ on q, we recall the basic definition of the deformation potential, for the LA mode and a spherical valley, as put forward by Bardeen and Shockley.[55] This is the idea that the change in energy of a carrier is proportional to the local dilation. In the notation of Eq. (13) this is

$$\delta E = (E_d + \tfrac{1}{3}E_u)\,\mathrm{Tr}\{\vec{\epsilon}\}, \tag{17}$$

where $\mathrm{Tr}\{\vec{\epsilon}\}$ is the dilation.

Alternately, we can express the dilation as $\vec{\nabla}\cdot\vec{u}$ with $\vec{u}$ a lattice displacement given by

$$\vec{u} = \hat{e}\left(\frac{N\hbar}{2\rho V\omega}\right)^{1/2} e^{i(\vec{q}\cdot\vec{r}-\omega t)}, \tag{18}$$

with V the crystal volume and N the phonon occupation number. Recalling that $\omega = vq$ for the acoustic-phonon modes of interest, we see that $\vec{\nabla}\cdot\vec{u}$ is proportional to $q^{1/2}$, and that $P(q)$, proportional to the square of the matrix element, is therefore linear in q.

The cutoff at $\vec{q} = 2\vec{k}_F$ can be understood geometrically as shown in the inset to Fig. 23(a) where the scattering process $\vec{k}_i + \vec{q} \rightarrow \vec{k}_f$ is schematically illustrated. The magnitude of $\vec{q}$, involved in the momentum transfer, is bounded by the electronic Fermi surface diameter $2\vec{k}_F$. This limitation was originally realized by Keldysh and has been further studied by Hensel and Dynes. The latter authors give evidence for such a cutoff using the heat-pulse method.[56]

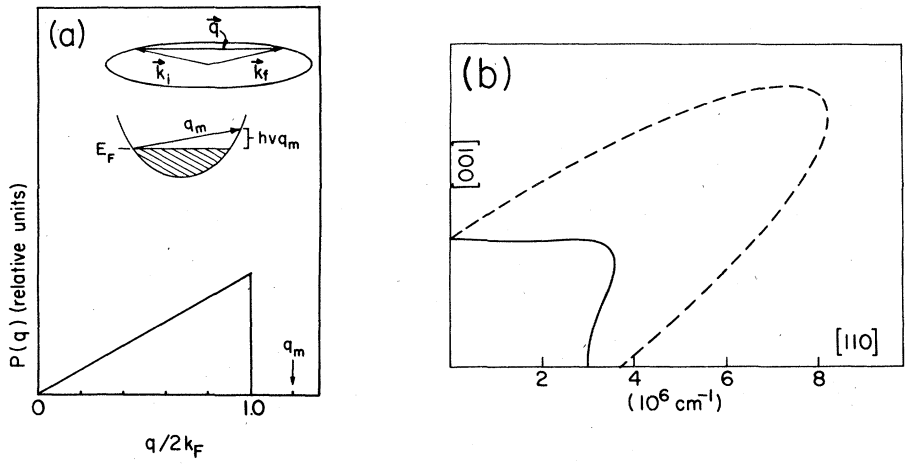

FIG. 23. The $2k_F(\hat{q})$ absorption cutoff factor. (a) The inset shows the geometric relations determining $q \leq q_m = 2k_F + 2mv/\hbar$. These relations are dictated by conservation of energy and momentum. The absorption probability $P(\vec{q})$ is sketched as a function of q, along $\langle 111\rangle$, assuming $\hbar\omega q \ll E_F$. For the EHD-LA case, $P(q)$ actually remains nonzero out to $q_m = (1.18)2k_F$ due to conservation of energy. (b) Polar plot of $\langle 2k_F\rangle$ (solid curve), and the maximum $2k_F$ (dashed curve) as a function of $\hat{q}$ in the $(1\bar{1}0)$ plane. Note that in this part of the $(1\bar{1}0)$ plane, the maximum $2k_F$ is identical to the value of $2k_F$ for the [111] valley.

One additional modification of this simple dependence is, however, required for the EHD system. The condition $E_F \gg \hbar\omega$ is not always satisfied. In contrast to the relatively large Fermi energies of ordinary metals, E_F for the electron-hole liquid is only $E_F^e = 2.5$ meV, comparable to the energy of the long-wavelength acoustic phonons of interest. (The average phonon energy in a Planck distribution at $T_p = 6$ K is 1.5 meV.) Therefore, we cannot neglect the energy of the phonon ($\hbar vq$) in the scattering process. Indeed, if we assume that the initial-state electron k vectors are limited to $\vec{k}_i \lesssim \vec{k}_F$, then conservation of energy requires that $q \leq 2k_F + 2mv/\hbar$. Here m is the electron effective mass in a given direction. The ratio $mv/\hbar k_F$ is therefore a measure of how far past $2k_F$ that $P(q)$ remains nonzero. We find that, for the LA mode[57] in Ge, this ratio has a maximum of 0.18 along $\langle 111\rangle$, and a minimum of 0.034 perpendicular to $\langle 111\rangle$. These ideas are illustrated in Fig. 23(a), where $P(q)$ is sketched for the LA phonons and the electrons in the drop. At the temperature of interest, $k_B T = 0.17$ meV or about 7% of E_F. This $k_B T$ broadening also tends to extend the nonzero range of $P(q)$. This latter broadening of E_F is not included in Fig. 23(a).

The Fermi surface of the electrons in the electron-hole liquid is quite anisotropic: it is an ellipsoid with eccentricity of $(m_l/m_t)^{1/2} = 4.4$, as shown in the inset to Fig. 23(a). This is the source of an anisotropy in the phonon-wind force on a droplet, $2k_F$ is greater along the [111] axis than along any other direction. Still, in a droplet, all four electron valleys are occupied. Thus, for a general direction there are four Fermi wave vectors of interest. To obtain an idea of the magnitude of this effect, we first calculate the average Fermi wave vector for the four valleys

$$\langle 2k_F \rangle = 2k_{F_0} \tfrac{1}{4} \left(\frac{m_l}{m_0}\right)^{1/2} \sum_i^4 \left(\cos^2\theta_i + \frac{m_l}{m_t}\sin^2\theta_i\right)^{-1/2} . \tag{19}$$

Here $2k_{F_0} = 2(3\pi^2 n_0 m_l/m_0)^{1/3} = 10.0 \times 10^6$ cm^{-1} is twice the Fermi wave vector along the major axis of a single ellipsoid, and the angle θ_i is defined by the relation $\cos\theta_i = \hat{q}\cdot\hat{a}_i$. The electron masses are taken as $m_l = 1.58 m_0$ and $m_t = 0.082 m_0$. This average $2k_F$ is plotted as the solid curve in Fig. 23(b). Another indicator of the anisotropy is the maximum $2k_F$ for a given direction of $\vec{q}$. This is plotted as the dashed curve in Fig. 23(b). Note that in this portion of the $(1\bar{1}0)$ plane, the maximum $2k_F$ is actually identical to the Fermi diameter of the [111] valley. Thus, in general, the maximum $\vec{q}$ that is absorbed depends on the orientation of $\vec{q}$ relative to the four Fermi surfaces. In the next section, it will become evident exactly where the anisotropy of $2\vec{k}_F(\hat{q})$ enters into the calculation of the phonon-wind force.

D. Phonon-wind-force calculation

In this section the factors in Eq. (8) are brought together and the nonradial phonon-wind force is calculated. To make the calculation tractable the following approximations are made: (1) The nonequilibrium phonon distribution function N_q^* is taken as in Eq. (9) with $A(\hat{r})$ defined by Eq. (11). (2) The $2k_F$ cutoff factor is taken as a sharp cutoff at $2k_F(\hat{q})$ for each valley. (3) The $|\vec{q}|$ dependence of the screened deformation potential is neglected.[58]

Given these simplifying approximations, an expression for the force $\vec{F}_\alpha(\vec{r})$ for each mode α, may be reduced to

$$\vec{F}_\alpha(\vec{r}) = \frac{F_0}{r^2} \sum_i^5 C_\alpha \int_0^{4\pi} d\Omega_q \hat{q}[\hat{q}\cdot\vec{D}\cdot\hat{e}_\alpha(\hat{q})]^2 A_\alpha(\hat{q})\delta(\hat{r}-\hat{q}) \times \int_0^{2k_{F_i}(\hat{q})} dq \frac{q^4 e^{\hbar v_\alpha q/k_B T_p}}{(e^{\hbar v_\alpha q/k_B T_p} - 1)^2} , \tag{20}$$

where the constant F_0 is independent of direction or mode and $v_\alpha(\hat{q})$ is the phase velocity in the $\hat{q}$ direction. It can now be seen that the anisotropy of $2k_F(\hat{q})$ modulates the upper limit of the radial integral in Eq. (20). This radial integral is proportional to the fourth Debye integral[59] $J_4(x)$ of argument

$$x = 2k_F(\hat{q})\hbar v_\alpha(\hat{q})/k_B T_p . \tag{21}$$

Finally, using $J_4(x)$ we rewrite Eq. (20) as

$$\vec{F}_\alpha(\vec{r}) = \frac{F_0}{r^2} \sum_i^5 C_\alpha \int_0^{4\pi} d\Omega_q \hat{q}_\alpha(\hat{q}\cdot\vec{D}\cdot\hat{e})^2 \left(\frac{k_B T_p}{\hbar v_\alpha}\right)^5 \times A_\alpha(\hat{q}) J_4(x(\hat{q}))\delta(\hat{r}-\hat{q}) . \tag{22}$$

This integral can be evaluated by taking advantage of the delta function defined below Eq. (11).

As mentioned previously, for the two TA modes there is often a degeneracy of $\vec{q}$ vectors associated with a given $\vec{V}$ direction. In Ge there are up to 11 $\vec{q}$ vectors for certain $\vec{V}$ directions.[41] In the present calculation, a complete table of all of the $\vec{q}$ vectors associated with a given $\vec{V}$ direction for each mode is first constructed using a two-dimensional root-finding scheme. From this table the phonon-wind force is calculated in the following manner: For each $\vec{q}$ entry in the table, Eq. (22) is evaluated using the delta function. The function $J_4(x)$ is evaluated by interpolation from a table.[59] The vector sum of the forces due to each $\vec{q}$ vector in the table is then computed. This sum is the force

for a particular mode and direction. This is performed independently for each of the three phonon modes. The total force is then the properly weighted vector sum of the contributions of the three phonon modes.[60]

The phonon-wind force, as calculated from Eq. (22), is sensitive to the value of the parameter T_p, the nonthermal phonon temperature. This sensitivity shows up in both the overall magnitude, and the relative anisotropy of the force. In the context of Eq. (22), this T_p dependence can be traced to the radial integral $J_4(x)$. This function is plotted in Fig. 24(a). Note that for $x \gtrsim 10$, $J_4(x)$ saturates, and that higher values of T_p will tend to lower the value of x to the region of the curve with a maximum slope. The modulation of $2k_F$ as a function of $\hat{q}$ in turn modulates the value of $J_4(x)$, and this last modulation is most prominent where $J_4(x)$ has a steep slope. Figure 24(b) shows $\sum_i^5 J_4(x; 2k_{Fi})$, for the LA mode, plotted as a function of $\hat{q}$ for three values of T_p. These curves are normalized to a value of unity at the [111] direction.[61] At higher T_p the anisotropy is greatly amplified while at lower T_p the saturation illustrated in Fig. 24(a) levels out this contribution to the $\hat{q}$ dependence. In all three plots of Fig. 24(b) the anisotropy is almost exclusively due to $2k_F(\hat{q})$. The LA phase velocity has only a weak ($\lesssim 10\%$) dependence[62] on $\hat{q}$. Thus, an anisotropic $2k_F(\hat{q})$ together with a "high" phonon temperature, modulate the value of $J_4(x)$, and therefore the calculated force. It should be noted that because the phase velocities of the TA modes are always smaller than the phase velocity of the LA mode,[63] this T_p enhanced anisotropy is stronger for the TA modes than for the LA mode.[64] Physically, this T_p dependence can be understood by examining the dependence on $\hat{q}$ of the number of phonons that can participate in the phonon-wind force. In Fig. 24(c) we plot the black-body power spectrum $U(q, T_p) \propto q^3[\exp(\hbar v q/k_B T_p) - 1]$ as a function of q for the LA mode and $T_p = 2$ and 6 K. The vertical lines at 2.4 and 10.0×10^6 cm^{-1} indicate the minimum and maximum values of $2k_F$ in the $(1\bar{1}0)$ plane. These occur at the [100] and [111] directions, respectively, and are obtained from Fig. 23(b). A measure of the T_p-dependent anisotropy is obtained from the ratio R of the total number of phonons below these two cutoffs. This is simply the ratio of the areas under the curve for $0 \leq q \leq 2k_F$. For $T_p = 2$ K this ratio is $R(2\text{ K}) = 1.43$ while for $T_p = 6$ K the ratio is $R(6\text{ K}) = 9.74$, and therefore $R(6\text{ K}/4\text{ K}) = 6.8$. Hence, the calculated anisotropy, due to the modulation of $2k_F(\hat{q})$, is enhanced at $T_p = 6$ K by a factor of 6.8 in this case. A value of $T_p = 6$ K was chosen because it produced calculated results best conforming to the experimental observations at high excitation level. In the rest of this paper $T_p = 6$ K will be assumed.

The magnitude of the phonon-wind force, evaluated at a constant radius, and calculated from Eq. (22), is plotted in a set of polar plots in Fig. 25. These plots give the log of the force as a function of direction in real space. In Fig. 25(a) the LA force is given, showing the broad maximum along [111]. For the LA mode, all of the contributing

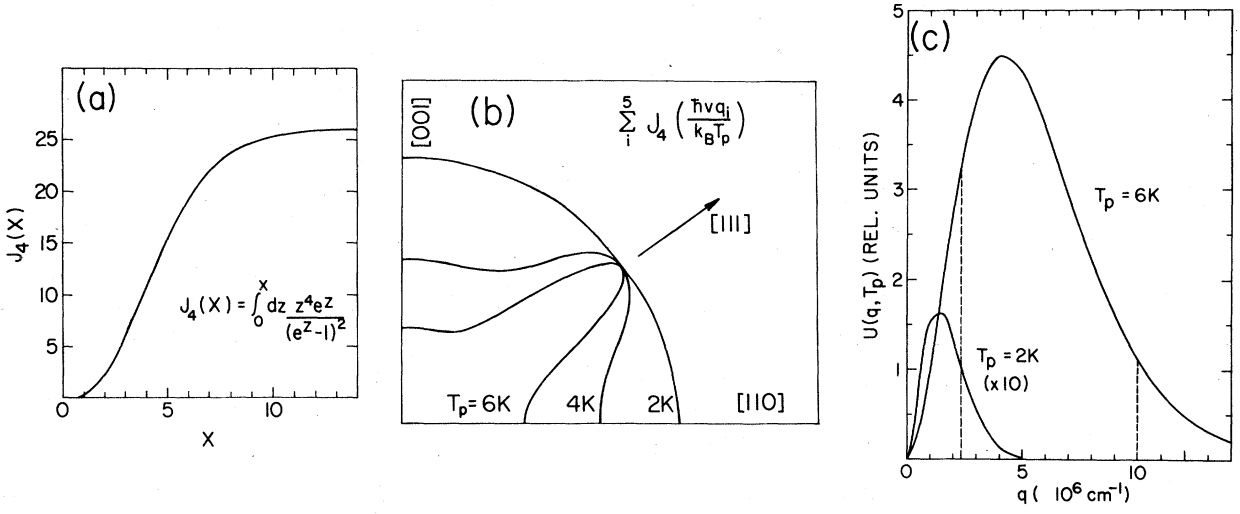

FIG. 24. T_p dependence of the cloud shape. (a) Plot of $J_4(x)$, the fourth Debye integral. (b) Polar plot of the sum of $J_4(x)$ for the LA mode over the four electron valleys plus the holes, as a function of $\hat{q}$. These curves for three T_p values are normalized at the [111]. The anisotropy of $2k_F(\hat{q})$ produces the observed anisotropy in $J_4(x)$. (c) Plot of $U(q, T_p) \propto q^3/[\exp(\hbar v q/k_B T_p) - 1]$ as a function of q for $T_p = 2$ and 6 K. The two vertical lines indicate the minimum and maximum values of $2k_F$ in the $(1\bar{1}0)$ plane for the LA mode.

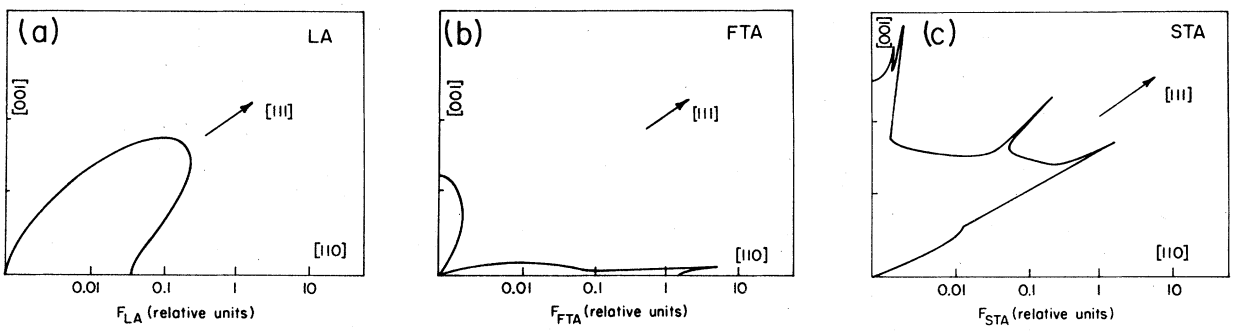

FIG. 25. Log polar plots of the components of the phonon wind force in the $(1\bar{1}0)$ plane as a function of $\hat{r}$. (a) LA force, (b) FTA force, and (c) STA force.

factors in the force possess a broad maximum near the $\langle 111 \rangle$ directions. The TA contributions to the force are displayed in Figs. 25(b) and 25(c). These last two plots demonstrate that the anisotropy of the TA force is dominated by the anisotropy contained in the phonon enhancement factor $A(\hat{r})$, as displayed in Figs. 19 and 20. Figure 25 illustrates that each of the three phonon modes makes a unique contribution to the calculated phonon-wind force, and confirms the identification of the central lobes and the two flare structures with specific phonon modes.

In Fig. 26 the predicted constant-density surface due to the total anisotropic-phonon-wind force from Eq. (22), summed over α, is plotted. Assuming a boundary condition of constant EHD density on the hemisphere $\frac{2}{3}\pi r_0^3$, this constant-density surface is proportional to $F^{1/3}$ evaluated at a constant radius. The constant-density boundary condition is an important factor in understanding why the cloud profile has a maximum extent where the force is a maximum: droplets are effectively supplied at the excitation region as fast as they are transported out into the crystal. In addition, in the real cloud near the TA singularities, droplets are swept out of the phonon path and channeled into the flare structures, further enhancing the prominence of the flares. The microscopic implications of this constant-density boundary condition are dealt with in detail in the discussion section. Figure 26 does not include a finite absorption length for the LA mode as in Figs. 16 and 17.

E. Droplet trajectories

In order to illustrate the nonradial nature of the phonon-wind force, Eq. (22) may be used to calculate droplet trajectories under the influence of the phonon-wind force. A droplet at a position $\vec{r}_0(t_0)$, at time t_0, will be pushed to a new position $\vec{r}(t_0+t)$ at a time t. With the drift velocity of Eq. (1), $\vec{V}_D = (\tau_p/M)\vec{F}$, the new droplet position is given by

$$\vec{r}(t_0+t) = \vec{r}_0(t_0) + (t_p \vec{F}/M)t. \tag{23}$$

Therefore, assuming an initial position $\vec{r}_0$, Eq. (23) can be iteratively solved to calculate droplet trajectories.

For this calculation, a table of the vector sum of the forces associated with each $\hat{V}$ direction is calculated in advance, and used in Eq. (23) for $\hat{F}$. The force table is constructed at a sufficiently dense set of group velocity directions to permit linear interpolation between the table entries, and the instantaneous radial distance $|\vec{r}|$ is used in calculating the $1/r^2$ fall off of the force. These calculations are performed in the $(1\bar{1}0)$ plane to take advantage of the fact that trajectories which start in this plane must, by symmetry, remain in the plane. The EHD are started on a hemisphere of $r_0 = 100$ μm, and trajectories are calculated in steps of $\Delta t = 10^{-8}$ s for times up to 40 μs, one

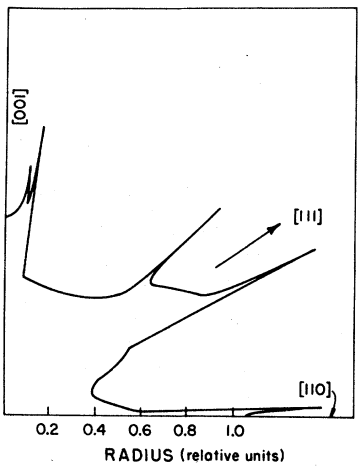

FIG. 26. Polar plot of a constant-density surface, calculated as $F^{1/3}$, in the $(1\bar{1}0)$ plane with all three phonon modes included in the force.

droplet lifetime.

Figure 27 presents these trajectories for each phonon mode separately and for the total force. Contours at constant time intervals are also plotted as the dashed lines. Trajectories are displayed for the LA mode in Fig. 27(a) and as can be seen, they tend to curve *away* from the [111] direction. Trajectories due to the FTA mode are shown in Fig. 27(b) and these again show the effect of conical refraction; the FTA mode provides no force for $40° \leq \theta \leq 70°$. At $\theta = 88.1°$ the direction and strength of the force abruptly change; droplets are pushed into the [110] axis. The break in the bottom line of Fig. 27(b) indicates the extent of the trajectory along [110]. In the real cloud the {100} planar flares are actually more spread out than predicted here. We postulate that this is due to the repulsive R-phonon interactions.

The contribution of the STA mode is illustrated in Fig. 27(c). Droplets are here swept into the ⟨100⟩ axes. In addition, the STA mode provides a force in the general direction of the [111] axis, in a sense complementing the FTA mode. Trajectories from the total force are shown in Fig. 27(d). Here we see the contributions from all three acoustic modes, the broad [111] lobes, the sharp [100] flares, and the very sharp {100} flares. Again, the break in the line along [110] indicates the extent of the trajectory along [110]. The inset illustrates the channeling of droplets into the {100} planes.

Although only Fig. 27(d) corresponds to a physically realizable situation (i.e., all three modes), the trajectory calculations in Figs. 27(a)–27(c) actually provide rather interesting information on $\vec{F}$ and $\vec{V}$. These calculated trajectories form a map of the relative orientation of $\vec{F}$ and $\vec{V}$, for each of the three phonon modes, while the *rate* at which the EHD traverse a specific trajectory is determined by the local magnitude of the phonon-wind force. Thus, the trajectories are somewhat analogous to stream lines in a steady-flow fluid problem, and provide a pictorial representation of the vector field $\vec{F}(\hat{r})$ for each phonon mode. From the perspective of phonon physics, it is interesting to note that the droplets are a unique, $\vec{q}$-vector sensitive, detector of ballistic phonons.

In this section the various contributing factors to the anisotropic-phonon-wind force have been examined. The phonon-wind force reflects the spatial anisotropy of both the phonon distribution and the carrier-phonon interaction. The nonradial nature of the force is displayed by calculating droplet trajectories. Figures 27(a)–27(d) are, in a sense,

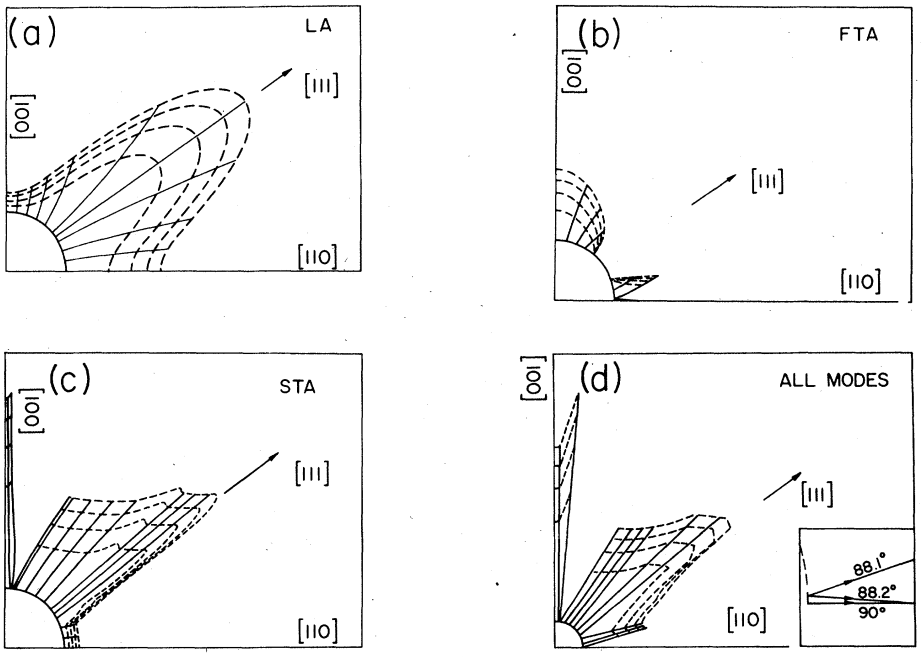

FIG. 27. Calculated EHD trajectories. From initial positions on the surface of a hemisphere of 100-μm radius, droplet trajectories, are iteratively calculated in the $(1\bar{1}0)$ plane. Constant time contours at 10-μs intervals are plotted as dashed lines. The trajectories are plotted at 10° intervals except near the symmetry directions. (a) LA force only. (b) FTA force only. The break in the bottom line indicates the extent of the trajectory along [110]. (c) STA force only. (d) Total force. Again, the break indicates the extent of the trajectory along [110]. The inset illustrates the channeling of droplets into the [110] direction. This channeling occurs throughout the {100} plane.

a single-particle picture; they illustrate the response of a single "test droplet" to the phonon force field generated at the excitation spot.

V. DISCUSSION

In this paper we have presented extensive experimental results on the steady-state EHD cloud in Ge, and a set of model calculations of the anisotropic-phonon-wind force. The various anisotropic features observed in the cloud have been illustrated, and the relative contributions of the various anisotropy factors of the phonon-wind force investigated. Each of the three main anisotropy features observed in the cloud in Ge, the lobes and the two sets of flares, can be identified with specific acoustic-phonon modes emanating from the localized excitations region.

We believe that the calculations of Sec. IV give a reasonably accurate description of the force on an electron-hole droplet which is well inside the crystal ($r \gg r_0$). Unfortunately, no experiment has yet been devised to directly measure the phonon-wind force at *one point* in the crystal. (The velocimetry measurements of Doehler and Worlock[14,15] come the closest to doing this, since $V_D = F\tau_p/M$; however, their laser sampled a slice through the crystal corresponding to many $\vec{r}$ directions.) Thus, we are relegated to measuring the *effects* of the phonon-wind force: How far are droplets pushed into the sample and what is their anisotropic density distribution? These questions involve the *cumulative* effect of the forces on a droplet from the moment of its creation near the excitation region to its gradual demise by recombination at the edge of the cloud. The problem of predicting the average cloud density $n_{av}(\vec{r})$ in a continuous excitation condition is thus much more complex than merely predicting forces well away from the excitation region. In particular, a model is required to approximate the particle dynamics very near the excitation region.

Fortunately, one of the simplest approximations for the excitation region works very well in explaining the measured droplet distribution, as attested to by the good agreement between the calculation of Fig. 17 and the data of Fig. 7(b). The assumption used in this calculation was that the excitation region consisted of a hemisphere of constant droplet or carrier density with volume $\frac{2}{3}\pi r_0^3$. The size and shape of this region is perhaps not so important as the assumption that the EHD density is not angular dependent, despite the anisotropic forces pushing droplets out of the excitation region. The implicit assumption is that as a droplet is removed from this region by phonon forces, its place in the excitation region is filled in by another droplet. This would seem to imply mutual interaction between droplets (via R phonons perhaps), or perhaps the existence of an electron-hole plasma near the excitation region.

The importance of this "fill-in effect" may be illustrated in a Gedanken experiment: initially create a uniform density of droplets over the surface of a hemisphere of radius r_0 and turn on an anisotropic-phonon-wind force $\vec{F}(\vec{r})$. Each droplet will then follow a well-defined trajectory; those with the larger force will travel farther into the crystal before decaying. A steady-state situation may be approximated by creating, at r_0, a new set of droplets at regular time intervals. Assuming radial forces, the density of droplets along any radius will then depend inversely upon the phonon-wind force, since the total number of droplets within a given solid angle is independent of angle. This is contrary to the experimental results, where directions of large EHD penetration into the crystal also corresponds to directions of high luminescence intensity, and thus high density.

A mechanism is thus needed to produce more droplets along strong force directions. This is mathematically accomplished by assuming a uniformly dense hemisphere at the excitation point, which implies fill in. The microscopic reasons behind this effect will have to rely upon detailed experimental investigations of the excitation region—not easy experiments.

Another important unknown factor is the energy distribution of the nonthermal phonon flux which is created by the thermalization of hot carriers. It seems hopeful that the new techniques of phonon spectroscopy which are currently being developed will contribute to a better understanding of the carrier thermalization phenomenon. Our quantitative analysis of electron-hole droplet clouds contains useful information toward this end: The cloud shapes are quite well explained by assuming a Planck distribution of nonthermal phonons with temperature between 5 and 10 K. In fact, these two simple assumptions concerning the excitation region and the phonon-distribution lead to a remarkably good theoretical agreement with the complex spatial distribution of electron-hole droplets in Ge.

ACKNOWLEDGMENTS

We acknowledge an ongoing interaction with R. S. Markiewicz who created the initial theory for the anisotropic-phonon-wind problem, and with G. A. Northrop who helped shape our ideas on the ballistic phonon flux and also provided several computer programs which were used in calculating the phonon force. M. Tamor provided essential help in

the initial interfacing of our imaging system with the LSI-11 microcomputer. We are grateful to E. E. Haller and W. L. Hansen of Lawrence Berkeley Laboratory who graciously provided the Ge samples and our detector crystal. This work was supported by NSF Grant No. DMR-77-11672. Equipment and facility support was also provided under Materials Research Laboratory Grant No. DMR-77-23999.

---

[1]See, for example, reviews by C. D. Jeffries, Science 189, 955 (1975); J. C. Hensel, T. G. Phillips, and G. A. Thomas, and T. M. Rice, *Solid State Physics*, edited by H. Ehrenreich, F. Seitz, and D. Turnbull (Academic, New York, 1977), Vol. 32.

[2]A. D. A. Hansen, T. Omyama, and J. L. Turney, *Proceedings of the International Conference on Applications of High Magnetic Fields in Semiconductor Physics* (Physikalisches Institut, Wurzburg, 1976).

[3]This inertial mass is the sum of the constituent masses $M=\frac{1}{3}m_l+\frac{2}{3}m_t+m_{hH}+m_{hL}=0.97m_0$, and was first noted in Ref. 13.

[4]The actual diffusion constant, due to impurity trapping of EHD, is much smaller. An upper limit of $D=10^{-9}$ cm^2/s was obtained by R. M. Westervelt *et al.*, Phys. Rev. Lett. 42, 267 (1979).

[5]Ya. E. Pokrovskii and K. I. Svistunova, Zh. Eksp. Teor. Fiz. Pis'ma Red. 13, 297 (1971) [JETP Lett. 13, 212 (1971)]; Fiz. Tverd. Tela (Leningrad) 13, 2788 (1971) [Sov. Phys.—Solid State 13, 2334 (1972)]; N. N. Sibeldin, V. S. Bagaev, V. A. Tsvetkov, and N. A. Penin, *ibid.* 15, 177 (1973) [15, 121 (1973)].

[6]J. M. Worlock, T. C. Damen, K. L. Shaklee, and J. P. Gordon, Phys. Rev. Lett. 33, 771 (1974); M. Voos, K. L. Shaklee, and J. M. Worlock, *ibid.* 33, 1161 (1974); J. C. V. Mattos, K. L. Shaklee, M. Voos, T. C. Damen, and J. M. Worlock, Phys. Rev. B 13, 5603 (1976).

[7]Ya. E. Pokrovskii and K. I. Svistunova, in *Proceedings of the Twelfth International Conference on the Physics of Semiconductors, Stuttgart, 1974,* edited by M. H. Pilkuhn (Teubner, Stuttgart, 1974), p. 71; Fiz. Tverd. Tela Leningrad 16, 3399 (1974) [Sov. Phys.—Solid State 16, 2202 (1975)]; R. W. Martin, Phys. Status Solidi B 61, 223 (1974); B. J. Feldman, Phys. Rev. Lett. 33, 359 (1974).

[8]J. Doehler, J. C. V. Mattos, and J. M. Worlock, Phys. Rev. Lett. 38, 726 (1977).

[9]L. V. Keldysh, Zh. Eksp. Teor. Fiz. Pis'ma Red. 23, 100 (1976) [JETP Lett. 23, 86 (1976)].

[10]V. S. Bagaev, L. V. Keldysh, N. N. Sibeldin, and B. A. Tsvetkov, Zh. Eksp. Teor. Fiz. 70, 702 (1976) [Sov. Phys.—JETP 43, 362 (1976)].

[11]R. S. Markiewicz, Solid State Commun. 33, 701 (1980); Phys. Rev. B 21, 4674 (1980).

[12]A. Elci, M. O. Scully, A. L. Smirl, and J. C. Matter, Phys. Rev. B 16, 191 (1977).

[13]J. C. Hensel and R. C. Dynes, Phys. Rev. Lett. 39, 969 (1977).

[14]J. Doehler and J. M. Worlock, Solid State Commun. 27, 229 (1978).

[15]J. Doehler and J. M. Worlock, in *Proceedings of the Fourteenth International Conference on the Physics of Semiconductors, Edinburgh, 1978,* edited by B. L. H. Wilson (The Institute of Physics, Bristol, 1978).

[16]M. Greenstein and J. P. Wolfe, Phys. Rev. Lett. 41, 715 (1978).

[17]R. S. Markiewicz, Phys. Status Solidi B 90, 585 (1978).

[18]M. Greenstein and J. P. Wolfe, Solid State Commun. 33, 309 (1980).

[19]M. A. Tamor and J. P. Wolfe, Phys. Rev. B 21, 739 (1980).

[20]P. Vashista, S. G. Das, and K. S. Singwi, Phys. Rev. Lett. 33, 911 (1974).

[21]M. Altarelli and N. O. Lipari, Phys. Rev. Lett. 36, 619 (1976).

[22]J. P. Wolfe, W. L. Hansen, E. E. Haller, R. S. Markiewicz, C. Kittel, and C. D. Jeffries, Phys. Rev. Lett. 34, 1292 (1975).

[23]The diode was fabricated at Lawrence Berkeley Laboratory by E. E. Haller. The detector housing was designed and constructed in our lab. To our knowledge the idea of using this type of detector for ir luminescence studies was first suggested by C. D. Jeffries. For further details see S. M. Kelso, Ph.D. thesis, University of California, Berkeley, 1979 (unpublished).

[24]The LSI-11/02 microcomputer is manufactured by the Digital Equipment Corporation, and the model G-300 PD optical galvanometer scanners are manufactured by General Scanning Inc.

[25]The Ge crystals were grown by E. E. Haller and W. L. Hansen of Lawrence-Berkeley Laboratory. Dislocation density is determined by a decorative etch. See R. G. Rhodes, *Imperfections and Active Centers in Semiconductors* (Pergamon, New York, 1964), p. 353.

[26]M. Greenstein, J. P. Wolfe, and E. E. Haller, Solid State Commun. 35, 1011 (1980).

[27]Excitation surfaces were first lapped with 3.0-μm Al_2O_3 on a glass substrate, and then etched 1–2 min HNO_3:HF; 3:1. Those surfaces to be polished were again lapped and polished with diamond polishing compound to a final 1-μm grit size. This polishing procedure produces an optical quality surface.

[28]W. Dietche and H. Kinder, J. Low Temp. Phys. 23, 27 (1976).

[29]D. J. Evans and S. Ushioda, Phys. Rev. B 9, 1638 (1974).

[30]A previous attempt to measure the dependence of droplet velocities on excitation energy, Ref. 15, was interpreted as a null result. That experiment was done with a defocused excitation, producing smaller clouds, and was discussed in Ref. 18.

[31]In this experiment the transmission factors for all of the optics involved were accounted for. The absorption factors were obtained from R. F. Potter, Phys. Rev. 150, 562 (1966). The reflectivity values of this reference were also checked experimentally at $T=2$ K.

[32]In both the etched and polished cases the Ar^+ source produces slightly larger penetration depths. For the polished surface R_Z tends to increase with power,

reaching 1.2 at $P_{inc} = 150$ mW.

[33]This figure was published previously in Refs. 26 and 34.

[34]R. S. Markiewicz, M. Greenstein, and J. P. Wolfe, Solid State Commun. 35, 339 (1980).

[35]By symmetry these cannot be {100} planar flares.

[36]An axial structure must remain invariant under rotation about its axis.

[37]H. J. Maris, J. Acoust. Soc. Am. 50, 812 (1971).

[38]B. Taylor, H. J. Maris, and C. Elbaum, Phys. Rev. B 3, 1462 (1971).

[39]F. Rösch and O. Weis, Z. Phys. B 25, 101 (1976); 25, 115 (1976).

[40]G. A. Northrop and J. P. Wolfe, Phys. Rev. Lett. 43, 1424 (1979).

[41]G. A. Northrop and J. P. Wolfe, Phys. Rev. B 22, 6196 (1980).

[42]J. C. Hensel and R. C. Dynes, Phys. Rev. Lett. 43, 1033 (1979).

[43]J. P. Wolfe, M. Greenstein, and G. A. Northrop, *Proceedings of the Fifteenth International Conference on the Physics of Semiconductors, Kyoto, 1980* (The Society for Atomic Collisional Research, Kyoto, 1980).

[44]See, for example, J. M. Ziman, *Electrons and Phonons*, 2nd ed. (Oxford University Press, Oxford, 1979), p. 357.

[45]P. Taborek and D. Goodstein, Solid State Commun. 33, 1191 (1980).

[46]This figure was published previously in Ref. 34. For this calculation a more sophisticated calculation of N_q^* was actually used. See Ref. 11.

[47]The elastic constants are taken as c_{11}, c_{12}, $c_{44} = 131.1$, 49.2, 68.2×10^{10} dynes/cm^2, $\rho = 5.34$ g/cm^3, from H. J. McSkimin and P. Andreatch, J. Appl. Phys. 34, 651 (1963).

[48]A fundamental assumption of phonon-focusing theory is an isotropic distribution of $\vec{q}$ vectors.

[49]J. de Klerk and M. J. D. Musgrave, Proc. Phys. Soc. London B68, 81 (1955). See also, Refs. 37 and 41.

[50]A computer program provided by G. A. Northrop was used for the two-dimensional root finding.

[51]G. E. Pikus and G. L. Bir, in *Symmetry and Strain-Induced Effects in Semiconductors*, edited by D. Louvish (Halstead, New York, 1974).

[52]H. Brooks, Adv. Electron. 7, 85 (1955).

[53]C. Herring and E. Vogt, Phys. Rev. 101, 944 (1956).

[54]The equivalence of Eqs. (13) and (14) can be shown with Eqs. (15) and (16).

[55]J. Bardeen and W. Shockley, Phys. Rev. 80, 72 (1950).

[56]J. C. Hensel and R. C. Dynes, in *Proceedings of the Fourteenth International Conference on the Physics of Semiconductors, Edinburgh, 1978,* edited by B. L. H. Wilson (The Institute of Physics, Bristol, 1978).

[57]For the TA modes this ratio has a maximum of 0.096 along ⟨111⟩, and thus the cutoff is at 1.096 of $2k_F$.

[58]This is equivalent to assuming that $k_{TF}^2/q^2 \ll 1$, i.e., the perfect screening limit. The correction is small; see, Refs. 11 and 17.

[59]W. M. Rogers, R. L. Powell, Natl. Bur. Stand. (U.S.) Circ. No. 595 (1958).

[60]The normalization constant C_α is the total number of phonons of mode α created by a Planck distribution with $T = T_p$. Thus, C_α is the integral over d^3q of the product of the density of states and the distribution function

$$C_\alpha = \int d^3q\, DN \propto \frac{1}{\langle v_\alpha^3 \rangle} .$$

The ratios of $1/\langle v_\alpha^3 \rangle$ for the three modes are LA : FTA : STA = 1.0 : 3.7 : 5.4.

[61]The ratios of absolute magnitudes at the [111] are 2 K : 4 K : 6 K = 3.3 : 1.6 : 1.0.

[62]The LA phase velocities at the symmetry directions are 5.0, 5.4, and 5.6×10^5 cm/s in the ⟨100⟩, ⟨110⟩, and ⟨111⟩ directions, respectively.

[63]The FTA phase velocities are 3.56, 3.56, and 3.06×10^5 cm/s, and for the STA are 3.56, 2.77, and 3.06×10^5 cm/s, in the ⟨100⟩, ⟨110⟩, and ⟨111⟩ directions, respectively.

[64]This is because for a given T_p, x_{TA} is smaller than x_{LA} since $v_{TA} < v_{LA}$.

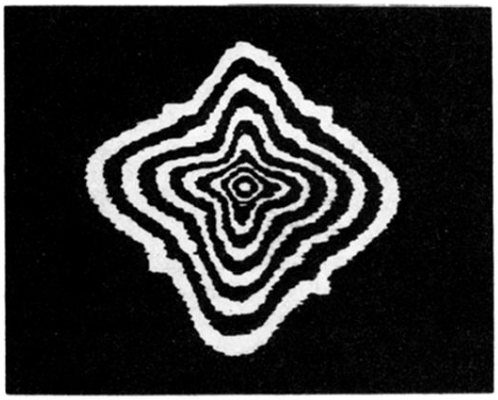

(a)

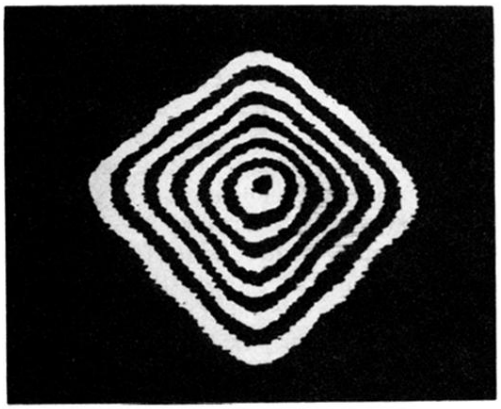

(b)

FIG. 10. Focus dependence of the cloud shape. P_{inc} = 76 mW as in Fig. 7, Δx = 2.3 mm. (a) Laser spot diameter = 300 μm. (b) Laser spot diameter = 500 μm.

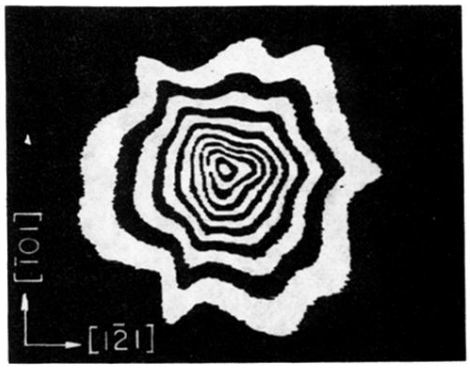

(a)

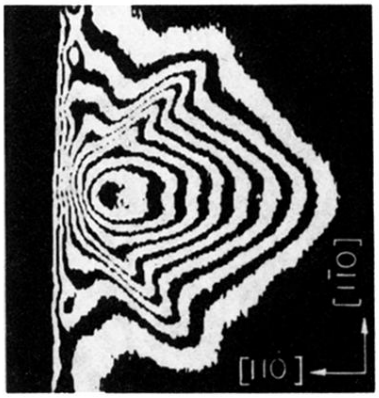

(b)

FIG. 11. (a) Excitation on a (111) surface, face view, $\Delta x = 3.5$ mm, $P_{\text{inc}} = 76$ mW. (b) Excitation on a polished surface (110), [001] viewing direction. The laser strikes the crystal at the left. This image corresponds to the excitation geometry for the slit-scan data in Fig. 4; $\Delta x = 1.6$ mm, $P_{\text{inc}} = 15$ mW.

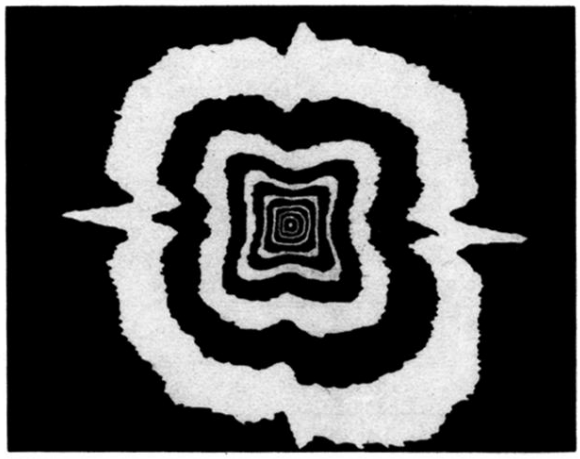

FIG. 12. Rotation experiment. Sample was rotated 20° about the [001] (vertical) axis. $P_{\text{inc}} = 228$ mW, $\Delta x = 2.5$ mm.

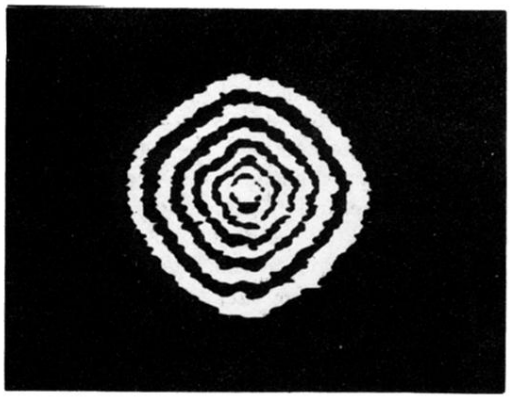

(a)

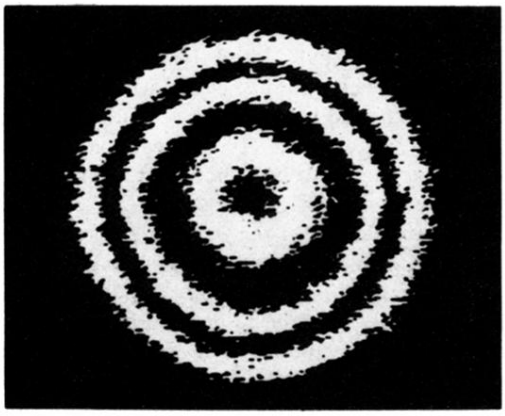

(b)

FIG. 15. 4.2 K data. (a) Spectrally resolved EHD image at $T = 4.2$ K, $\Delta x = 3.2$ mm, $P_{\text{inc}} = 23$ mW. (b) Spectrally resolved FE image at $\lambda = 1.738$ μm and $T = 4.2$ K. $\Delta x = 5.0$ mm, $P_{\text{inc}} = 57$ mW.

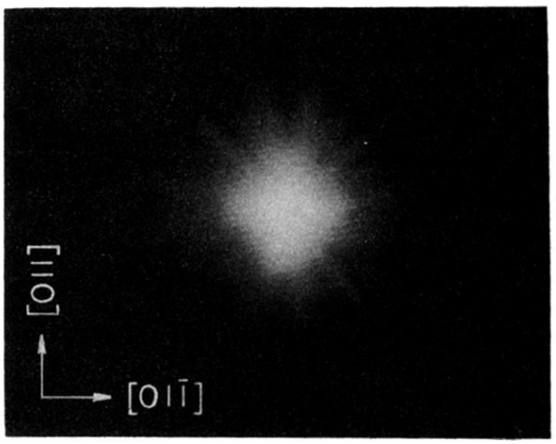

(a)

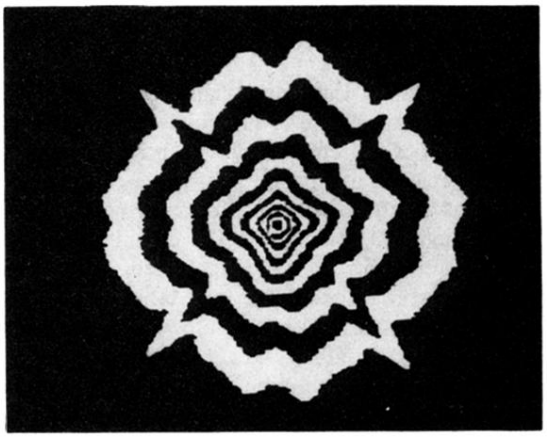

(b)

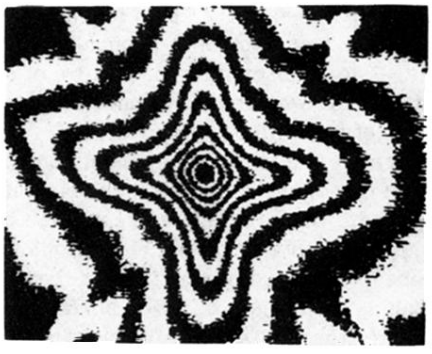

(c)

FIG. 7. Infrared image of the EHD cloud produced by focused excitation on a (100) etched surface, and viewed through the ($\bar{1}$00) surface. The photo width is $\Delta x = 2.5$ mm, $P_{inc} = 76$ mW. (a) Image as displayed on a storage oscilloscope. (b) Contour map; the alternating black and white bands connect contours of constant intensity. (c) Contour map of the central region of the cloud, $\Delta x = 1$ mm.

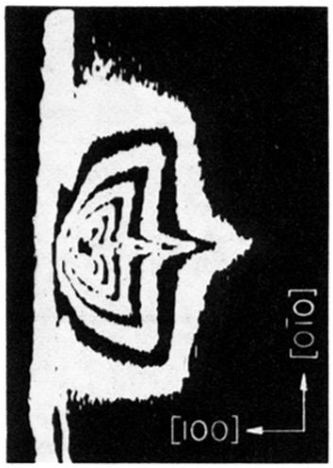

(a)

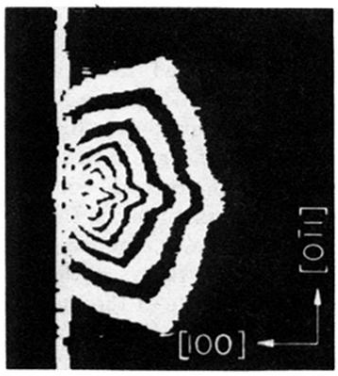

(b)

FIG. 8. Side view of the [100] pumped cloud $P_{inc} = 76$ mW. The laser excites the crystal from the left. The vertical line is the excitation surface. (a) Viewed along [001], $\Delta x = 5.4$ mm. (b) Viewed along [011], $\Delta x = 6.5$ mm.

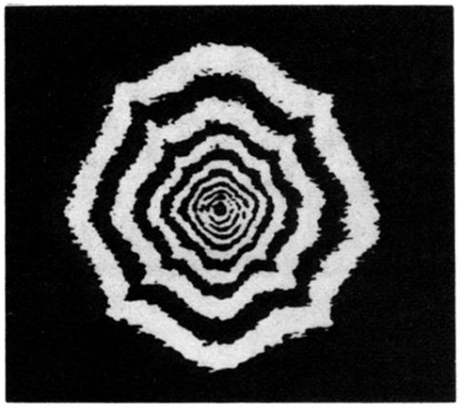

(a)

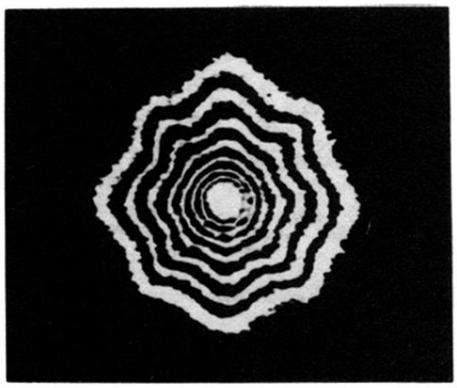

(b)

FIG. 9. Power dependence of the cloud shape for focused excitation on an etched (100) surface. (a) $P_{\mathrm{inc}} = 7.6$ mW, $\Delta x = 2.5$ mm. (b) $P_{\mathrm{inc}} = 2.3$ mW, $\Delta x = 2.0$ mm.